

Exploiting a Mixture-of-Layers in an Electrocardiography Foundation Model

Phu X. Nguyen*, Huy Phan[‡], Hieu Pham[§], Christos Chatzichristos*, Bert Vandenberg^{†¶}, and Maarten De Vos^{*||}

*STADIUS Center for Dynamical Systems, Signal Processing and Data Analytics, Department of Electrical Engineering (ESAT), KU Leuven, Leuven 3001, Belgium

[‡]Meta Reality Labs, Paris 75002, France

[§]VinUni-Illinois Smart Health Center, VinUniversity, Hanoi, Vietnam

[†]Department of Cardiovascular Sciences, KU Leuven, Leuven 3001, Belgium

[¶]Department of Cardiology, University Hospitals Leuven, Leuven 3001, Belgium

^{||}Department of Development & Regeneration, KU Leuven, Leuven 3001, Belgium

Abstract—Transformer-based foundation models for Electrocardiograms (ECGs) have recently achieved impressive performance in many downstream applications. However, the internal representations of such models across layers have not been fully understood and exploited. An important question arises: Does the final layer of the pre-trained Transformer model, the *de facto* representational layer, provide optimal performance for downstream tasks? Although our answer based on empirical and theoretical analyses for this question is negative, we propose a novel approach to leverage the representation diversity of the model’s layers effectively. Specifically, we introduce a novel architecture called Post-pretraining Mixture-of-layers Aggregation (PMA), which enables a flexible combination of the layer-wise representations from the layer stack of a Transformer-based foundation model. We first pre-train the model from ECG signals using the 1-dimensional Vision Transformer (ViT) via masked modeling. In downstream applications, instead of relying solely on the last layer of the model, we employ a gating network to selectively fuse the representations from the pretrained model’s layers, thereby enhancing representation power and improving performance of the downstream applications. In addition, we extend the proposed method to the pretraining stage by aggregating all representations through group-wise averaging before feeding them into the decoder-based Transformer. Extensive experimental results demonstrate that our proposed models outperform other self-supervised learning (SSL) baselines on various arrhythmia classification benchmarks with different settings (i.e., in-distribution and out-of-distribution datasets). The proposed approaches obtain a macro AUC exceeding 94% for 71 ECG conditions and show strong generalization across different application settings. Our detailed analysis further consolidates and underscores the crucial role of the multi-layer representation mixture.

Index Terms—Electrocardiography (ECG), Masked Vision Transformer, Self-Supervised Learning, Foundation Model.

I. INTRODUCTION

Cardiovascular disease (CVD) is the leading cause of death globally, accounting for 32% of all deaths according to The World Health Organization (WHO) statistics in 2019 [1]. With its non-invasive nature and ability to reflect the heart’s

electrical activity, the electrocardiogram is a key diagnostic tool in clinical practice [2], [3]. However, traditional ECG analysis is mainly based on human experts prone to errors and delays. Deep learning models with a supervised learning paradigm [4]–[22] have shown effectiveness in automating ECG analysis and aiding CVD diagnosis. The supervised learning paradigm, however, faces inherent limitations such as reliance on large-scale annotated data, lack of generalization ability, and susceptibility to data heterogeneity. To address these issues, self-supervised learning (SSL) methods have been proposed. These methods leverage unlabeled ECG data to train robust foundational models, which are then fine-tuned for specific downstream tasks. This approach promises improved generalization and reduced reliance on manually annotated data.

Self-supervised ECG learning (eSSL) generally includes two primary methods: contrastive learning [23]–[29] and generative learning [30]–[35]. The former learns by pulling together similar pattern representations and pushing apart different pattern representations. It is often based on data augmentation techniques, as a result, frequently distorts the semantic meaning of the original ECG signal [35]–[37]. In contrast, the latter learns by reproducing the original signal, thereby retaining more semantic information. It is better at preserving the semantic information in ECG data, as it learns data representation by reconstructing all or part of the original input. However, the generative approach also has its own issues. By reconstruction-based learning, it often overlooks high-level semantics which are crucial for downstream tasks. This can lead to suboptimal performance when using generative pre-trained models for classification [35], [37]–[39].

Contrastive predictive coding of the ECG (CPC) was explored in [40]. Unlike the contrastive approaches above, CPC predicts multiple future time steps using powerful autoregressive models in the latent space [41]. The goal is to force the model to focus on the global structure and disregard low-level information. Furthermore, the CPC method does not require complicated augmentations, thus preserving the semantic information of the ECG data. Despite these advantages, this

[‡]The work does not relate to H. Phan’s position at Meta.

method heavily relies on negative samples. The model might fail to learn meaningful representations if negative samples lack diversity. Additionally, CPC typically employs autoregressive models (e.g., recurrent neural networks) for future predictions, which can make capturing long-range dependencies challenging. To learn global information and preserve the semantic meaning of ECG signals, Transformer-based architectures have been utilized in [31]–[35], thanks to their attention mechanism.

Recently, SSL-based ViT models have been increasingly used for ECG foundation models. In this line of work, the representation obtained from the last layer of a pretrained model has been the default for downstream tasks. No studies have yet examined the representation power of the intermediate layers for downstream tasks. We will show that the layers of a pretrained ViT model often exhibit diverse distributions, and there is no guarantee that the last layer provides the best representation for the downstream tasks. Our analyses show that the representation power is lowest in the first layers, increases and peaks in the middle layers, and then decreases slightly towards the last layers. Motivated by this, we explore ViT’s intermediate layers as alternatives to the last layer for downstream tasks. We then propose methods, both in-pretraining and post-pretraining, to dynamically aggregate the representations across different layers of a ViT model to produce the collective representation.

Our contributions are as follows.

- Through empirical and theoretical analyses, we illuminate the representation power of intermediate layers of a pretrained ViT model for ECG downstream tasks.
- We propose post-pretraining aggregation methods based on (i) pooling and (ii) a Mixture of Layers model to fuse the representations from different layers of a pretrained ViT model for ECG downstream tasks.
- In the pre-training task, we further investigate the impact of aggregating intermediate representations from different layers in the ViT model encoder before feeding them to the Transformer decoder.
- Through extensive experiments, we show that (i) our proposed models outperform SSL baselines on various downstream arrhythmia classification benchmarks with different settings (i.e., in-distribution vs. out-of-distribution, linear probing vs. fine-tuning) and that (ii) the learned representations are meaningful for ECG signals.

II. THE BACKBONE MODEL

A. 1-Dimensional Vision Transformer (ViT1d)

ECG signals are usually long time series. Directly applying the conventional Transformer model at each time point significantly increases the computational costs due to its self-attention mechanism and limits the ability to exploit important morphological features of the signal. ECG beats, such as the P, T, and U waves, contain clinically meaningful shape information that can be overlooked if the model processes the signal only at the time point level rather than in contextual segments. In this paper, we employ as the backbone network a 1-dimensional ViT for fixed-length 12-lead ECG signals [35].

1) *Patch Embedding*: Denote an input ECG signal as $\mathbf{X} \in \mathbb{R}^{C \times L}$, where C is the number of leads and L is the length of the ECG signal. We split the ECG signal into 1D non-overlapping segments called ECG patches and denoted by

$$\mathbf{X}_p \in \mathbb{R}^{C \times N \times P}, \quad (1)$$

where $N = \lfloor \frac{L}{P} \rfloor$ is the number of patches and P is the length of a patch, respectively. ECG patches are then projected into D -dimensional patch embeddings using a linear projection:

$$\mathbf{Y}_0 = \mathbf{X}_p \mathbf{W}_e + \mathbf{b}_e, \quad (2)$$

where $\mathbf{Y}_0 \in \mathbb{R}^{C \times N \times D}$, $\mathbf{W}_e \in \mathbb{R}^{P \times D}$, and $\mathbf{b}_e \in \mathbb{R}^D$.

2) *Positional Encoding and Lead Encoding*: A shared embedding, denoted as $[SEP]$, is inserted before and after the sequence of patch embeddings to support the model in distinguishing between patch embeddings from different leads, \mathbf{Y}_0 , resulting in

$$\mathbf{Y}'_0 = [[SEP] \ \mathbf{Y}_0 \ [SEP]] \in \mathbb{R}^{C \times (N+2) \times D}. \quad (3)$$

To effectively model the ECG features, we add the learnable positional embeddings to the patch embeddings:

$$\mathbf{Y}''_0 = \mathbf{Y}'_0 + \mathbf{E}_{pos}. \quad (4)$$

To improve the discriminative capability among leads, the learnable lead embeddings are added to \mathbf{Y}''_0 as follows

$$\mathbf{Y} = \mathbf{Y}''_0 + \mathbf{E}_{lead}, \quad (5)$$

3) *Transformer Encoder*: We stack 12 Transformer layers in the encoder, where each layer comprises three components:

- Multi-head Self-Attention (MSA)

$$\text{MSA}(\mathbf{Y}) = \text{Concat}(\text{head}_1, \dots, \text{head}_h) \mathbf{W}^O, \quad (6)$$

where each head is computed by a softmax function as follows

$$\text{head}_i = \text{softmax} \left(\frac{\mathbf{Q}_i \mathbf{K}_i^\top}{\sqrt{d_k}} \right) \mathbf{V}_i, \quad (7)$$

where $\mathbf{Q}_i = \mathbf{Y} \mathbf{W}_i^Q$, $\mathbf{K}_i = \mathbf{Y} \mathbf{W}_i^K$, $\mathbf{V}_i = \mathbf{Y} \mathbf{W}_i^V$, $\mathbf{W}_i^Q, \mathbf{W}_i^K, \mathbf{W}_i^V \in \mathbb{R}^{D \times d_k}$, $\mathbf{W}^O \in \mathbb{R}^{h \cdot d_k \times D}$.

- Add & Norm:

$$\mathbf{Y}^{(l)'} = \text{LayerNorm} \left(\mathbf{Y}^{(l-1)} + \text{MSA} \left(\mathbf{Y}^{(l-1)} \right) \right). \quad (8)$$

- Feed Forward Network (FFN):

$$\text{FFN}(x) = \text{GELU}(\mathbf{x} \mathbf{W}_1 + \mathbf{b}_1) \mathbf{W}_2 + \mathbf{b}_2, \quad (9)$$

$$\mathbf{Y}^{(l)} = \text{LayerNorm} \left(\mathbf{Y}^{(l)'} + \text{FFN}(\mathbf{Y}^{(l)'}) \right). \quad (10)$$

B. Masked Vision Transformer

Based on [35], the ECG patches are randomly masked in the pre-text task. The unmasked patches are fed into the ViT encoder, while the masked patches are reconstructed through the decoder-based Transformers as illustrated in Figure 1.

1) *Encoder*: In the pre-training phase, a random masking strategy is applied on the embedding sequence to reduce the inherent redundant information in the ECG signal and simultaneously avoid overfitting. For ease of presentation, we denote the unmasked embeddings as

$$\mathbf{Y}''_{0-unmask} = \{\mathbf{Y}''_{0(0)}, \mathbf{Y}''_{0(i_1)}, \dots, \mathbf{Y}''_{0(i_S)}, \mathbf{Y}''_{0(N+1)}\},$$

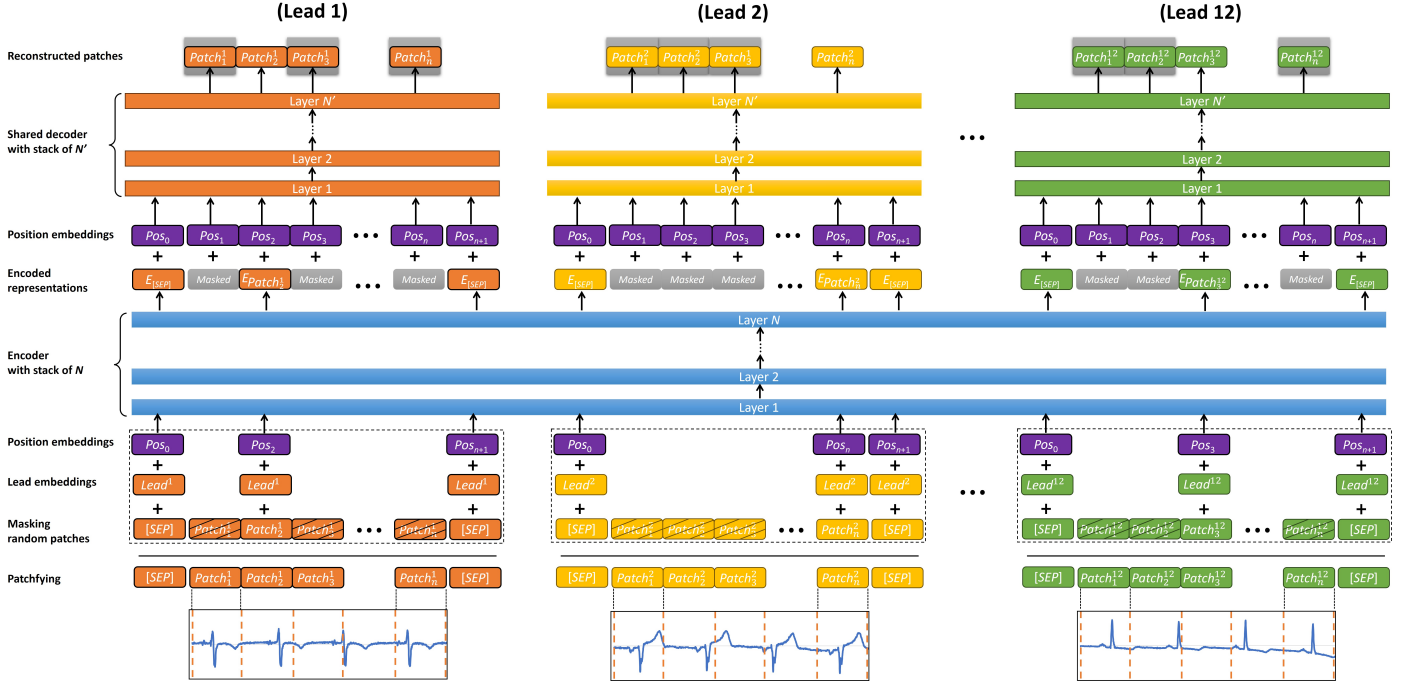


Fig. 1: The overview of Spatio-Temporal Masked Electrocardiogram Modeling (STMEM) [35].

and the masked embeddings as

$$\mathbf{Y}_{0-mask}'' = \{\mathbf{Y}_{0(j_1)}'', \dots, \mathbf{Y}_{0(j_{S'})}''\},$$

where $\mathbf{Y}_{0(0)}''$ and $\mathbf{Y}_{0(N+1)}''$ are embeddings resulted from $[SEP]$ tokens, S and S' are the number of unmasked and masked embeddings, respectively, with $S+S' = N$ and a masking ratio $m = \frac{S'}{N} \in [0, 1]$. Note that i_s and $j_{s'}$ are randomly selected from the embedding sequence, not including $[SEP]$ tokens. The unmasked embeddings are input to the Transformer layers for representation learning, whereas the masked embeddings will be employed as the reconstruction targets.

The learnable lead embeddings are added to the unmasked ECG embeddings as in (5):

$$\mathbf{Y}_{unmask} = \mathbf{Y}_{0-unmask}'' + \mathbf{E}_{lead}. \quad (11)$$

The ECG embeddings are then fed into the stack of Transformer layers to output the encoded embeddings as in (6)-(10)

$$\bar{\mathbf{Y}} = \text{Encoder}(\mathbf{Y}_{unmask}). \quad (12)$$

2) *Decoder*: The decoder receives the encoded embeddings. These embeddings are first projected into D' -dimension embeddings using linear projection:

$$\mathbf{Z}_0 = \bar{\mathbf{Y}}\mathbf{W}_d + \mathbf{b}_d, \quad (13)$$

where $\mathbf{W}_d \in \mathbb{R}^{D \times D'}$, $\mathbf{Z}_0 \in \mathbb{R}^{C \times (S+2) \times D'}$. A learnable shared mask embedding, $\mathbf{E}_{mask} \in \mathbb{R}^{C \times S' \times D'}$, is then shuffled into \mathbf{Z}_0 to create an expanding sequence, $\mathbf{Z}_{cat} \in \mathbb{R}^{C \times (N+2) \times D'}$, and reconstruct the original order of the elements, as in the original ECG embedding. Similarly to the encoder, the learnable positional embeddings are also added to \mathbf{Z}_{cat} to provide positional

information.

$$\mathbf{Z} = \mathbf{Z}_{cat} + \mathbf{E}_{decoder-pos}. \quad (14)$$

The embedding sequence, \mathbf{Z} , is sent to the shared lead-wise decoder with four additional Transformer blocks to reconstruct the masked segments. The training objective aims to minimize the error between the original ECG signals of the masked segments, $\{\mathbf{X}_i\}_{i \in \mathcal{M}}$, and their corresponding reconstruction output by the decoder, $\{\hat{\mathbf{X}}_i\}_{i \in \mathcal{M}}$

$$\mathcal{L}_{reconst} = \frac{1}{|\mathcal{M}'|} \sum_{i \in \mathcal{M}'} \|\hat{\mathbf{X}}_i - \mathbf{X}_i\|_2^2, \quad (15)$$

where \mathcal{M}' is the set of masked locations.

The shared lead-wise decoder is deliberately designed for multi-lead ECG. The spatio-temporal patchifying enables the decoder to access unmasked embeddings from multiple leads, all aligned with the same temporal information. Thus, the training process may become too simple, resulting in a negative impact on the representation of the encoder. To address this limitation, the decoder is designed to process the embedding sequence from each lead independently. This guarantees that the decoder does not directly exploit information from other leads during the reconstruction process. Such a design choice increases the task's difficulty, encouraging the encoder to learn the spatio-temporal representation more efficiently.

III. EFFECT OF HIDDEN LAYERS OF PRE-TRAINED ViTs

A. Linear probing evaluation across layers:

The results presented in Figure 2 show that the representations at the final layers of the model do not provide

optimal performance for the downstream classification tasks. The performance improves gradually from the early layers, peaks at the middle layers, and degrades at deeper layers. This trend is consistently observed across multiple evaluation metrics, datasets, and pre-trained models (i.e., STMEM and IPASTMEM) as shown in Appendix B, indicating the generality of the phenomenon. Thus, we can conclude that the middle layers of the Transformer provide richer representations. This is mainly because the representations at early layers are still raw and discrete, reflecting the uncertainty of information [42]–[45]. In the middle layers, the models begin to accumulate and aggregate information in depth, allowing it to learn the hidden relationships between different components of the signal, such as the morphological correlation between the ECG waves (P, QRS, T) and their associated time intervals, thus creating highly generalizable representations that are more suitable for downstream tasks. At deeper layers, the mutual information between features is degraded as the model shifts its optimal goal to reconstruct the original signal, thereby reducing the value of the representation for the classification task. Due to the quasi-periodic temporal nature of ECG signals, maintaining sequential relationships between feature components, such as the P wave, QRS complex, and T wave, is particularly important for models to learn long-term electrophysiological trends of cardiac activity. However, in addition to global temporal relationships, local features play an essential role in diagnosis, especially for short-term abnormalities such as conduction disturbances, premature beats, or QRS complex morphological distortions. Therefore, it is necessary to effectively utilize the multilayer representations of Vision Transformer to maximize the diversity and complementarity between feature levels, from local details in the shallow layers to abstract representations in the deep layers, thereby improving the model’s overall performance for the ECG signal classification task.

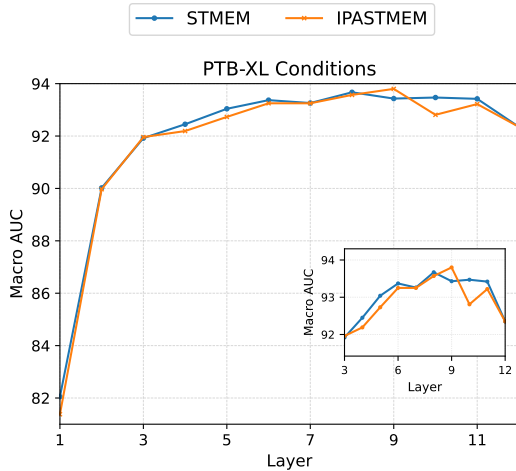


Fig. 2: PTB-XL Condition Classification: Layer-wise Macro AUC.

B. Average cosine similarity:

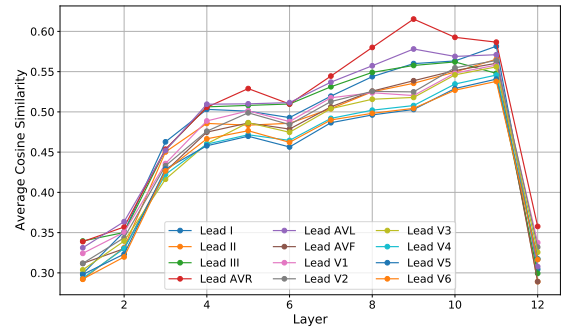
We use average cosine similarity to measure the degree of correlation between patch embeddings at each layer in pre-

trained ViT. This metric reflects the structure of the ECG signal representation because the ECG components inherently have close physiological dependencies (such as the relationship between P-QRS-T). Therefore, if the patches in the feature space show reasonable correlation, the model has learned an informative representation consistent with the nature of the signal.

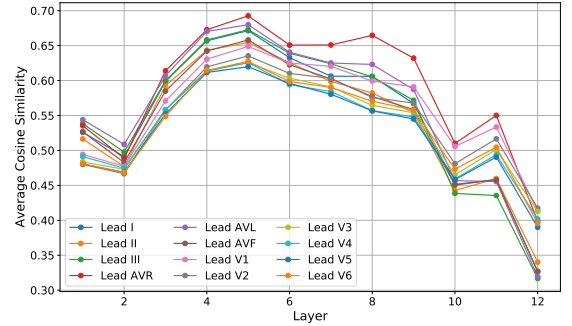
$$\text{CosSim}(\mathbf{h}_i, \mathbf{h}_j) = \frac{\langle \mathbf{h}_i^{(l)}, \mathbf{h}_j^{(l)} \rangle}{\|\mathbf{h}_i^{(l)}\| \|\mathbf{h}_j^{(l)}\|}, \quad (16)$$

The average cosine similarity between all different patch pairs (excluding self-similarity) at layer l -th is given by

$$\text{AvgSim}^{(l)} = \frac{1}{N(N-1)} \sum_{i=1}^N \sum_{j=1, j \neq i}^N \text{CosSim}(\mathbf{h}_i^{(l)}, \mathbf{h}_j^{(l)}). \quad (17)$$



(a) STMEM



(b) IPASTMEM

Fig. 3: Average cosine similarity on individual leads through inner layers of pre-trained ViT models.

Figure 3 illustrates the consistent variation of the average cosine similarity at each ECG lead across the hidden layers of the pretrained models (e.g., STMEM and IPASTMEM), clearly reflecting the information extraction process and convergence in the representation space. Specifically, the average cosine similarity value between patches of the same lead tends to increase from the early layers, peaks in the middle layers, and decreases in the last layers. This trend reflects the gradual synthesis of local information, where patches with close spatial and temporal relationships are increasingly represented more homogeneously. This is consistent with the observations shown

in previous studies [46], [47] about representation convergence in the deep layers of the Transformer. In particular, this phenomenon is entirely useful in representing the temporal and spatial information of ECG signals. However, [46] and [47] also warn that if not well controlled, the Transformer architectures may fall into an over-smoothing state, meaning that the patches become too similar, leading to representation saturation and reduced discrimination ability. In this context, applying reconstruction loss in the pre-training phase of both pre-trained models plays a key role in preventing the over-smoothing phenomenon and maintaining the fine-grained patterns of the representation at the last layers. As a result, the model retains the ability to distinguish between patches and better captures the characteristic spatiotemporal correlation of the ECG signal. The clear separation of the representation at the last layers also contributes to the model's ability to pay attention to local features, which are also necessary in ECG analysis. The comparison between the two models (Figures 5a and 5b) reveals a significant difference in the representation organization. STMEM exhibits a gradual convergence process, with patch similarity steadily increasing across layers before dropping sharply in the final layers. IPASTMEM achieves a high similarity early on (layers 4–5) and then gradually declines. This suggests that IPASTMEM tends to “compress” information at the beginning of the network, then re-establishes representational diversity in later layers. Notably, these properties are consistently maintained across all ECG leads, confirming that the model's representation learning mechanism does not depend on the individual characteristics of each signal channel but instead exhibits a generalization tendency across the entire input data space. Thus, pre-trained ViT models in multi-lead ECG signal processing demonstrate the high stability and adaptability. The results of the average cosine similarity across layers explain the phenomenon observed in the linear probing evaluation across layers: the middle layers often offer superior performance for downstream tasks. The reason is that the model reaches an optimal information synthesis state at this stage, in which the representations effectively encode the specific spatiotemporal relationship of the ECG signal.

Figure 4 visualizes cosine similarity maps between a query patch and other remaining patches in the representation layer of the ViT encoders pre-trained on a 12-lead electrocardiogram (ECG) signal. The input signal is 10 seconds long and divided into 20 patches containing 50 data points. In the illustration, a patch on lead V2, marked with a red border, is selected as the query, and the maps represent the cosine correlation between this patch and all other patches on all leads. Regarding space, the highly correlated regions are mainly concentrated in the precordial leads, specifically V1 to V6, which can be explained by the anatomical location of the query patch in lead V2, allowing the model to exploit features within the same anatomical structure preferentially. This result confirms the ability of pre-trained models to learn and represent spatial anatomical relationships between leads, even when the input signal is defined as discrete patches. Regarding time, highly

correlated patches with the query often exhibit similar ECG waveforms, reflecting the periodicity of physiological signals, a crucial factor in clinical diagnosis. In addition, it is observed that there is a clear difference between the two training strategies, with STMEM exhibiting a higher generalization ability across a wide range of correlations throughout the entire signal, both in space and time. In contrast, IPASTMEM primarily focuses on exploiting information from leads belonging to the same group as the query patch and is less spread out than STMEM, thus enhancing the ability to identify distinct fine-grained features in specific anatomical regions. These results support the hypothesis that ViT can learn complex spatio-temporal relationships in ECG signals and demonstrate that attention representations in the model's hidden layers can provide valuable explanatory information, making an essential contribution to developing explainable deep learning systems in the biomedical domain.

C. Average attention entropy:

Assume that at layer l , there are H attention heads and N patch embedding, each attention vector $\mathbf{a}_i^{(l,h)} \in \mathbb{R}^T$ is given by

$$\sum_{j=1}^N \mathbf{a}_{ij}^{(l,h)} = 1 \quad (18)$$

Entropy of a single attention vector $\mathbf{a}_i^{(l,h)}$ is defined as

$$H(\mathbf{a}_i^{(l,h)}) = - \sum_{j=1}^N \mathbf{a}_{ij}^{(l,h)} \log \mathbf{a}_{ij}^{(l,h)} \quad (19)$$

Average attention entropy (AAE) at layer l , computed across all tokens and heads, is given by

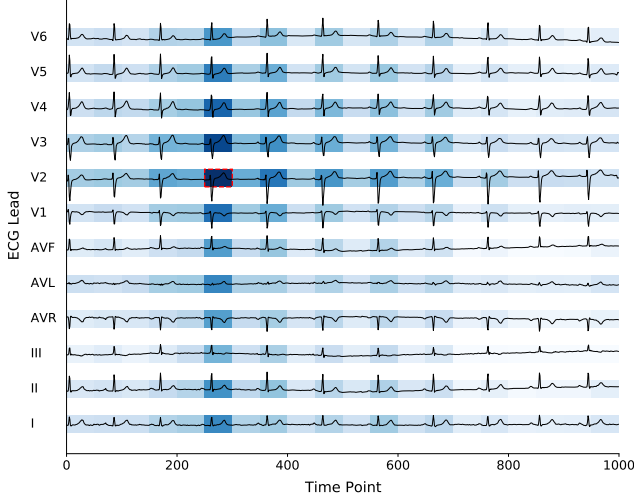
$$\text{AAE}^{(l)} = - \frac{1}{H \cdot N} \sum_{h=1}^H \sum_{i=1}^N \sum_{j=1}^N \mathbf{a}_{ij}^{(l,h)} \log \mathbf{a}_{ij}^{(l,h)} \quad (20)$$

To normalize the entropy to the range $[0, 1]$, we divide by the maximum possible entropy, which is $\log T$:

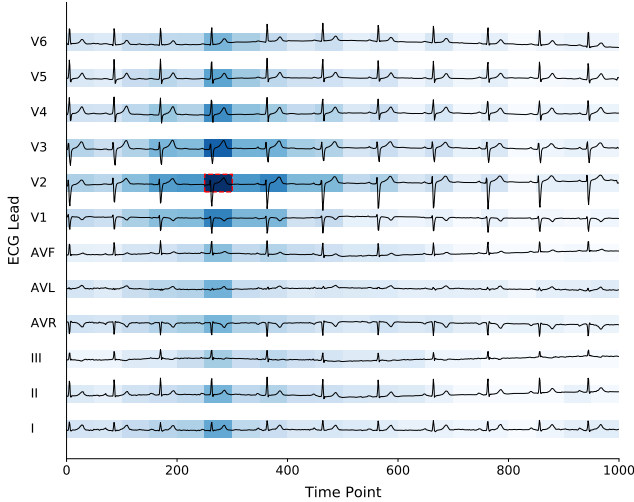
$$\text{AAE}^{(l)} = \frac{1}{H \cdot N \cdot \log T} \sum_{h=1}^H \sum_{i=1}^N \sum_{j=1}^N -\mathbf{a}_{ij}^{(l,h)} \log \mathbf{a}_{ij}^{(l,h)} \quad (21)$$

The results in Figure 3 show that at the final layer, the average cosine similarity between the patches drops significantly, returning to a level similar to that of the first layer. In Figure 5b, the average cosine similarity in the final layer is even lower than in the first layer. However, the linear probing results at each hidden layer of the two pre-trained models in Appendix A clearly show that the final layer still achieves significantly higher performance than the first layer, reflecting that the representation at the final layer has not degraded in quality. This suggests that the decrease in cosine similarity in the final layer does not imply a return to a “raw” representation but rather reflects a trend toward increased representational differentiation, where the model focuses on more local and fine-grained features in the ECG signal. Thus, average cosine similarity mainly provides information about the structural variation of representation between layers in the pretrained ViT,

but it is not a strong enough measure to confirm the quality of representation at each layer. This metric only reflects the level of internal coherence. To further support this observation, we analyze the attention entropy in each layer of both models (e.g, STMEM and IPASTMEM), to clarify the differentiation in the model’s attention level and scope according to depth.



(a) STMEM



(b) IPASTMEM

Fig. 4: Cosine similarity maps of 12-lead ECG provide whole spatial and temporal information regarding the heart: precordial leads (V1-V6) and limb leads (I, II, III, AVR, AVL, AVF). The above figure shows cosine similarity maps for a query patch (i.e., red dashed box) in lead V2 and the remaining patches in two pre-trained models: (a) STMEM and (b) IPASTMEM.

Analyzing the attention entropy in each layer, as shown in Figure 5, provides additional evidence to explain the performance degradation on downstream classification tasks when using the representation from the last layer. Both models exhibit very high entropy in the first layer, reflecting the dispersion of attention and the high uncertainty about the input information.

This is typical of the early stages of representation learning when the model has not yet identified the critical regions in the signal. From the second layer onward, the entropy drops rapidly. It stabilizes at a low level, indicating that the model begins to focus on meaningful information and the representation becomes more certain. In the final layers, the entropy increases slightly again, indicating that the model pays more attention to the fine-grained features in the ECG signal. However, the entropy level at the last layer is still significantly lower than at the first. When these observations are compared with the results from linear probing and cosine similarity, it can be concluded that the final layer is not a crude representation but rather a reconstruction stage designed to focus on high-resolution features.

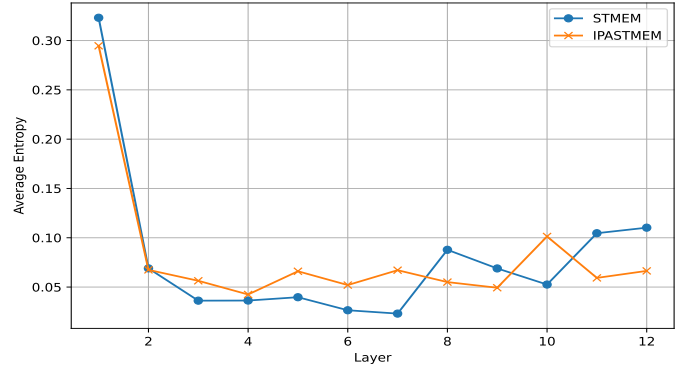


Fig. 5: Average attention entropy through inner layers of pre-trained ViT models.

IV. PROPOSED METHOD

As previously mentioned, we probe into the effect of individual inner layers of the pre-trained ViT model. Via linear probing evaluation, we find that different layers have uneven effects on the performance of downstream classification tasks, and that no single layer consistently outperforms across all tasks, datasets, and evaluation metrics. The optimal performance varies across the specifics of each task, dataset, and evaluation metric, with each layer outperforming in different contexts. Notably, the model’s last layer, commonly used in practice, does not provide optimal performance across most evaluation scenarios, while the highest efficiency usually appears in the middle layers. This phenomenon is caused by the change in the correlation level between input patches across the model layers. Specifically, the correlation between patches tends to increase from the early layers, converge in the middle layers, and decrease in the late ones. Due to the higher correlation level in the middle layers, the representations at this stage are often rich, thereby providing optimal performance for many downstream tasks. This correlation can be quantified through cosine similarity. We observed through experimental and mathematical analysis that in pretrained ViT built by masked modeling, “the average cosine similarity between ECG patches increases gradually from the early layers, converges in the middle layers, and

decreases in the last layers.” The mathematical analyses are presented in Appendix A.

Each layer in the ViT tends to learn information at different abstraction levels; early layers typically focus on low-level features, middle layers learn high-level semantic information, and deeper layers capture more fine-grained patterns. Therefore, multilayer fusion offers significant benefits: the model can simultaneously exploit fine-grained features and global context, improving the quality of the representation, reducing overfitting, and increasing the ability to generalize across ECG data from different sources [48]–[51]. In this study, we attempted to leverage the collective representations from different inner layers of the pre-trained model to derive a unified representation more likely to generalize to downstream tasks than the individual layers. Specifically, we investigated three schemes: post-pretraining pooling-based aggregation (PPA), post-pretraining mixture-of-layers aggregation (PMA), and in-pretraining pooling-based aggregation (IPA).

A. Post-pretraining Pooling-based Aggregation (PPA) - Scheme I

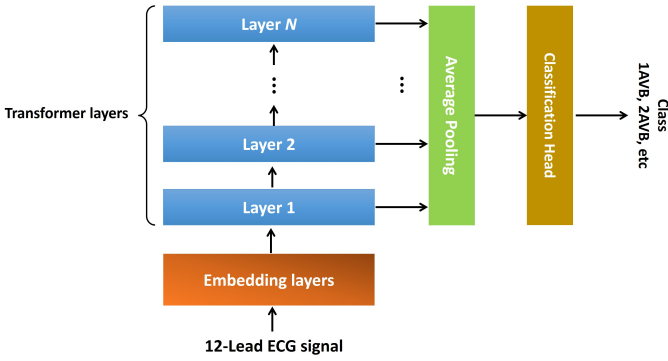
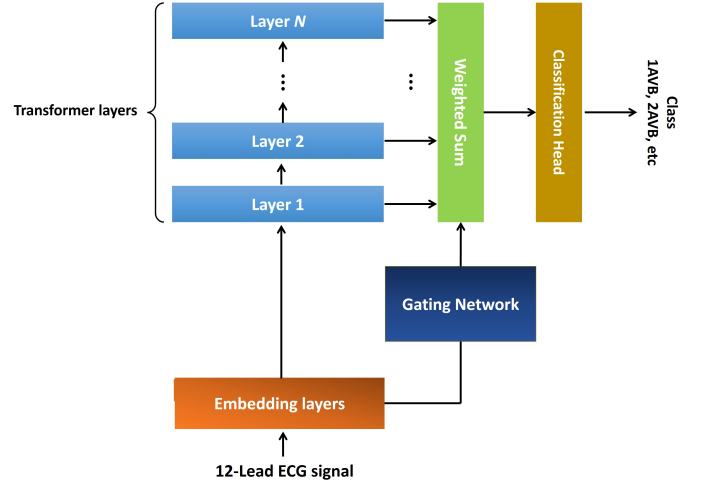


Fig. 6: Overview of post-pretraining pooling-based aggregation of the pre-trained ViT’s different layer-wise representations.

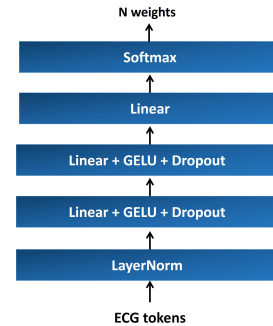
In this scheme, we apply the original ViT architecture and the training strategy presented in [35] during the pre-training stage. Unlike conventional methods, which typically only utilize the output from the last layer of the pre-trained ViT model to feed into the classification head, we propose a more comprehensive feature extraction strategy for the fine-tuning stage. Specifically, instead of relying only on the information from the deepest layer, we collect features from all inner layers of the pre-trained ViT model. These features are then combined through a simple but effective aggregation operation called average pooling to produce a unified and semantically rich representation that fully reflects the levels of abstraction learned by the model. The resulting aggregated representation from this pooling process is then fed into the classification head for classification, as shown in Figure 6. This method enables the simultaneous utilization of information at different representational layers, thereby enhancing the ability to recognize and distinguish signal patterns in the output dataset.

B. Post-pretraining Mixture-of-layers Aggregation (PMA) - Scheme II

The PPA method aggregates information from all layers in the pre-trained ViT through average pooling. In practice, it is difficult to determine which layer plays the most crucial role, since the performance of each layer can vary significantly depending on the specific dataset and classification task. Furthermore, some layers may produce inefficient representations, negatively affecting the overall performance. Using average pooling by default assigns equal weights to all layers. This leads to a lack of distinction between informative and poor representations, limiting the model’s generalization ability across different tasks and datasets. Inspired by the Mixture of Experts (MoE) architecture [52], [53], we propose to view each layer in ViT as an independent expert, each providing a unique feature representation. To solve the problem of selecting and weighting the output representations, we design a gating network that learns to focus on the layers containing rich information while minimizing the impact of the layers that do not contribute much value. This mechanism helps the model better adapt to the diversity of the dataset and improve the overall representation efficiency.



(a) Mixture of layers (MoL) architecture.



(b) Gating network.

Fig. 7: Overview of post-pretraining mixture-of-layers aggregation of pre-trained ViT’s different layer-wise representations.

The gating network inputs the ECG token sequences after the embedding layer. It applies a series of processing layers, including layer normalization (LayerNorm), three consecutive Linear-GELU-Dropout blocks, a final linear layer, and Soft-max to normalize the weights in a probability-oriented manner. The result is a weight vector of length N , corresponding to the number of layers in the Transformer, which determines the relative contribution of each layer to the final representation. The weighted ensemble representation is then fed into a classification head, which consists of a Fully Connected layer, to infer the output class labels corresponding to different types of heart disease in the ECG classification task. This structure allows the model to learn to selectively exploit information from the most relevant classes while minimizing the influence of classes with poor representations, thereby improving the ability to generalize across different datasets and tasks. The detailed architecture is shown in Figure 3.

C. In-pretraining Pooling-based Aggregation STMEM (IPASTMEM) - Scheme III

We propose an improved architecture for the ViT encoder by aggregating the inner layers in the pre-training stage of the STMEM, as illustrated in Figure 8. Exploiting and combining information from different layers helps improve the model's representation ability and efficiency in the self-supervised representation learning process.

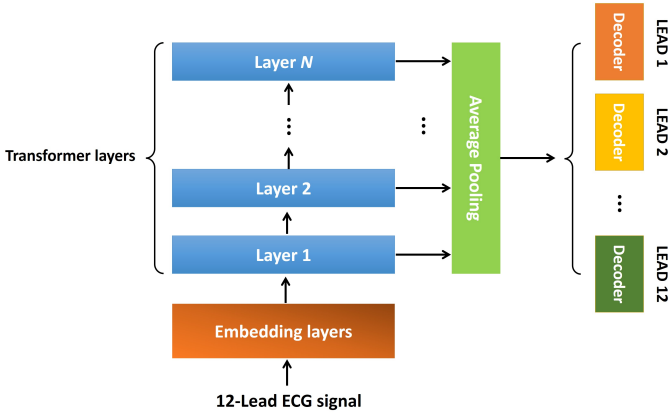


Fig. 8: Overview of the in-pretraining pooling-based aggregation STMEM (IPASTMEM).

In traditional settings, when only the last layer is passed to the decoder, it can easily lead to vanishing gradients or imbalances in parameter updates between layers. In contrast, applying the aggregation mechanism allows information and discrepancy signals to spread more evenly across the entire architecture, promoting a more stable and efficient optimization process. In particular, in masking-based pretraining methods, such as STMEM, the model must reconstruct masked input parts based on the remaining information. To perform this task effectively, having an informative feature representation synthesized from multiple layers in the encoder is a key factor. This integrated representation provides the detailed features

necessary to recover the occluded regions accurately. It helps the model learn the complex structural relationships between elements in the input, including local and global contexts. Effectively utilizing such multilayer representations is crucial for improving the quality of representation learning during the pre-training stage.

D. Downstream classification

In the training phase for the downstream classification task, we retain the encoder of the masked ViT models (e.g., STMEM and IPASTMEM) and then remove the $[SEP]$ tokens before feeding the representation vector into a classification head. Finally, we add a simple classification head with basic layers, such as batch normalization, dropout, ReLU, and a linear layer to map the output representation to the target labels. The model is applied to the multilabel classification problem on different datasets to identify ECG conditions and heart rhythm types.

The model's input data is a 12-lead ECG signal with a duration of 10 seconds. This signal is first fed into the encoder to extract the representation vector. Then, this vector is fed into the classifier to predict cardiovascular conditions, $\{\hat{o}_1, \dots, \hat{o}_K\}$. The loss function used during training is defined as follows:

$$\mathcal{L}_{CE} = \frac{1}{K} \sum_{c=1}^K (-o_c \log(\hat{o}_c)), \quad (22)$$

where $\mathbf{o} = \{o_1, \dots, o_K\}$ denotes the actual multi-label target and K is the number of labels.

V. EXPERIMENTAL SETTINGS

In this section, we describe in detail the experimental settings in this paper, including the implementation method, the baseline models, and the datasets used for our experiments.

A. Datasets

TABLE I: Summary of the datasets.

Dataset	Samples	Sample rate	Duration
Pretraining: All	400,365	multiple	multiple
- CinC2020 [54]	43,093	multiple	multiple
- Chapman [55]	10,646	500 Hz	10s
- Ribeiro-test [5]	827	400 Hz	7s, 10s
- CODE-15 [56]	345,799	400 Hz	7s, 10s
Evaluation:			
- PTB-XL [57]	21,8375	100 Hz, 500 Hz	10s
- Chapman [55]	10,646	500 Hz	10s

This paper utilizes five 12-lead ECG datasets collected from various countries and demographics for pre-training and downstream tasks. To ensure consistency throughout the training and evaluation process, all ECG signals are normalized to the same input format with a fixed sampling rate of 100 Hz and a signal length of 10 seconds. Specifically, recordings with durations exceeding 10 seconds are truncated. Conversely, shorter signals are zero-padded to ensure a standard length, facilitating consistent model building and training across datasets.

In the pre-training phase, the model was trained on a combined set of four datasets, namely PhysioNet / Computing

in Cardiology Challenge 2020 (CinC2020) [54], Chapman (Zheng) [55], CODE-test (Ribeiro2020) [5], and CODE-15 [56], with a total of 400365 records. For the downstream phase, the models are fine-tuned in two datasets, PTB-XL [57] and Chapman, to evaluate the fitness and generalizability of the learned representations on different datasets and settings.

It is essential to note that the CinC2020 dataset is compiled from five different data sources, including PTB-XL. We set up two separate training scenarios on the downstream classification task to evaluate the generalization of pre-training models: in-distribution and out-of-distribution on the PTB-XL dataset. Specifically, in the in-distribution scenario, the original version of CinC2020 is kept intact, including data from PTB-XL, and used to train the pre-trained models. In contrast, in the out-of-distribution scenario, the PTB-XL dataset is removed from CinC2020 before training, and PTB-XL is only used in the downstream phase. This experimental design enables us to evaluate the model’s dependence on the training data and its generalization ability when presented with an unseen data distribution during the pre-training phase. All datasets are summarized in Table I.

B. Training and evaluation

In the pre-training phase, the models are trained completely unsupervised (i.e., without using any labels) to learn informative feature representations from ECG data. After completing the pretraining process, the pre-trained models are fine-tuned and evaluated on two labeled datasets, PTB-XL and Chapman, representing prosperous clinical data sources. In this phase, we build two classification scenarios that reflect common application goals in practice: (1) classifying all ECG conditions and (2) classifying ECG rhythms, illustrated in Table II. This approach allows for a comprehensive evaluation of the model’s performance and adaptability in classification scenarios of varying complexity.

Since each ECG record may simultaneously exhibit multiple pathological features, including background conditions and arrhythmias, or even carry no diagnosis, the classification tasks are set up as multi-label classification. This setting reflects the complex nature of real clinical data. It places higher demands on the model in learning and distinguishing co-occurring manifestations of the same signal. To ensure the experimental results’ objectivity, reproducibility, and reliability, the datasets are divided into 10 non-overlapping sets, following a standardized partitioning strategy. Specifically, sets 1 to 8 are used for training, 9 for validation, and 10 for the testing set [40].

To ensure the experimental results’ reliability, stability, and reproducibility, we further designed the evaluation process to control for the random factor in training. Specifically, the entire experiment was repeated with 10 different random seed values, applied to all classification scenarios and datasets used. This repetition enables us to assess the model’s stability against fluctuations caused by weight initialization. Thus, the reported results reflect the average performance of the model and clearly

show the degree of variation in each setup, thereby contributing to the improvement of the reliability and objectivity of the entire experimental evaluation. On the other hand, to comprehensively evaluate the performance of the proposed methods, we apply a diverse set of evaluation metrics, designed to reflect the model’s performance on various aspects of the multi-label classification problem. In previous studies, model performance evaluation often focused on only one group of metrics, tended toward macro metrics, or used only sample-level metrics. Such assessments are likely to lead to a lack of comprehensiveness, because each metric type only reflects a particular aspect of model performance. To overcome this limitation, we simultaneously used macro-level and sample-level metrics in this study to provide a more comprehensive and multidimensional evaluation perspective. Specifically, we use the following metrics: macro area under the curve (AUC), sample AUC, instance accuracy, sample accuracy, macro F1-score, sample F1-score, macro mean average precision (mAP), and sample mAP.

C. Implementation Details

Evaluating the effectiveness of our proposed self-supervised learning model requires a comprehensive benchmarking system with various baseline methods. In this study, we establish a set of baseline models representing three major approaches in machine learning for electrocardiogram (ECG) signals, including supervised learning from scratch, contrastive learning, and generative learning.

TABLE II: ECG Conditions and Rhythms in PTB-XL and Chapman Datasets.

Dataset	ECG Conditions	ECG Rhythms
PTB-XL	71	12
Chapman	67	11

In the group of supervised learning models, we implement and evaluate three popular baseline architectures: the 1-dimensional XResnet50 (XResnet1d50), a hybrid architecture consisting of 4FC, LSTM, and 2FC (4FC+2LSTM+2FC), as introduced in [8], [40], and ViT1d [35], [58]. These models are trained from scratch on standardized ECG datasets (e.g., PTB-XL condition, PTB-XL rhythm, Chapman condition, and Chapman rhythm), without any pre-training knowledge, to reflect their ability to learn representations from raw data without the advantages of weight initialization. In particular, the XResnet model is selected due to its efficiency in processing one-dimensional signals. At the same time, ViT represents a state-of-the-art Transformer architecture in the field of vision, and 4FC+2LSTM+2FC demonstrates the ability to exploit temporal information to predict the next context. For XResnet1d50 and 4FC+2LSTM+2FC, we use the AdamW optimizer with a fixed learning rate of 0.001 and a weight decay factor set to 0.001. Training is performed with a binary cross-entropy loss function for multi-label classification, using a constant learning rate schedule and a batch size of 128. For the ViT1d model, training

is performed according to the configuration described in Table III (Fine-tuning section), but we use a smaller batch size, namely 16 in this case.

For the group of contrastive learning models, we examine typical methods such as Simple Contrastive Learning (SimCLR) [59] and Contrastive Predictive Coding (CPC) in the pre-training setting. These models are trained using popular loss functions in contrastive learning, such as noise contrast estimation (NCE) and InfoNCE loss, which aim to maximize the similarity between the representations of positive pairs while distinguishing them from negative pairs. The optimization process uses the AdamW optimizer algorithm. The models are then fine-tuned on multi-label classification tasks to evaluate the generalizability of the learned representation. The implementation details in the pre-training phase are similar to the methods presented in [40]. However, in the fine-tuning phase, we use an input ECG signal of 10 seconds duration, instead of 2.5 seconds as in the fine-tuned models in [40].

In particular, within the generative learning group, we implement and evaluate the spatio-temporal Masked Vision Transformer (STMEM), which also serves as the foundation for our proposed self-supervised model. In generative learning, the STMEM and our proposed methods use the ViT backbone, where the ECG signal is partitioned into non-overlapping segments (patches) with a patch size of 50 signal points each. During pre-training, 75% of the patches are masked randomly, and the model is trained to reconstruct the masked patches by minimizing the Mean Squared Error (MSE) loss function between the original and reconstructed patches. The training process uses the AdamW optimizer with a cosine annealing learning rate scheduler, a choice that is stable and efficient in large model training settings. The implementation details are given in the Table III.

VI. EXPERIMENTS AND RESULTS

A. Experimental Results

We evaluate the ECG representations learned by the various methods using two popular strategies: linear probing and fine-tuning, applied in both in-distribution and out-of-distribution settings. Since the experiments are repeated with many random seed values and evaluated on various metrics, we use the paired t-statistical test to determine the significance of the differences between the proposed and baseline methods. The corresponding results are presented in Tables IV, V, VI, and VII. Experimental analyses demonstrate that the proposed methods significantly improve most evaluation metrics, indicating their superior performance compared to the baselines.

In-distribution evaluation: The results presented in Table IV show that the proposed methods, especially Scheme II and III, outperform the baseline methods in both evaluation settings in complex ECG condition classification: linear probing and fine-tuning. Specifically, in the linear probing setting, Scheme II achieves the highest values in metrics such as Macro AUC (93.44 ± 0.14), Sample AUC (97.22 ± 0.08), Macro F1 Score (24.73 ± 0.78), Sample F1 Score (69.93 ± 0.31), Macro mAP

(32.25 ± 0.6), and Sample mAP (82.28 ± 0.12) indicating that the learned representation from the model generalizes well even when using only a simple linear classifier. In the fine-tuning stage, the advantages of the proposed methods are even more evident. Scheme II continues to lead with the highest values in most metrics, including Macro AUC (94.07 ± 0.18), Sample AUC (97.6 ± 0.15), Sample Accuracy (98.03 ± 0.02), Macro F1 Score (27.87 ± 1.11), Macro mAP (34.8 ± 0.75), and Sample mAP (83.94 ± 0.24).

Table V summarizes the experimental results on the PTB-XL dataset with the task of rhythm classification. In the linear probing, Schemes II and III show outstanding results. Scheme II achieves the highest performance for the Sample Accuracy (98.32 ± 0.04) and Macro F1 Score (48.21 ± 4.17). At the same time, Scheme III excels in Sample AUC of (95.7 ± 0.12), Instance Accuracy of (86.34 ± 0.28), Sample F1 Score of (86.61 ± 0.25), Macro mAP of (55.36 ± 2.32), and Sample mAP of (89.54 ± 0.23). For fine-tuning, it can be seen that the SimCLR model achieves high performance on several metrics such as Sample AUC (97.32 ± 0.49), Instance Accuracy (89.05 ± 0.45), Sample Accuracy (98.53 ± 0.08), Sample F1 Score (89.89 ± 0.96), and Sample mAP (92.84 ± 0.93). These results show that SimCLR has good optimization capabilities at the individual level of pattern recognition. However, the proposed methods show a clear advantage when considering the macro metrics such as Macro F1 Score and Macro mAP, which better reflect the ability to discriminate between imbalanced classes (common in ECG data). Specifically, Scheme II achieves the highest Macro F1 Score (50.9 ± 2.73) and Macro mAP of 56.64 ± 2.78 , surpassing all reference methods. This suggests that our model can learn a more informative representation and has better generalization to the entire label distribution, not just the popular classes.

Analysis of the results on the Chapman dataset, which includes two tasks: condition classification in Table VI and rhythm classification VII, provides further insight into the model's performance in the context of a much smaller dataset. Although the smaller dataset size may reduce the generalizability of some baseline methods, the proposed method maintains stable and superior performance on many important metrics. Scheme II achieves the highest Macro F1 Score (22.97 ± 0.92) and Macro mAP (28.11 ± 0.91) for condition classification. In Chapman rhythm, Scheme III achieves the highest Macro F1 Score (61.0 ± 3.24) and Macro mAP (64.75 ± 1.99), while Scheme II continues to lead in Sample AUC, Instance Accuracy, Sample Accuracy, Sample F1 Score, and Sample mAP. These results show that the proposed models learn a robust instance-level representation and discriminate well between uncommon labels – a common challenge in small biomedical datasets.

Overall results in in-distribution settings on both PTB-XL and Chapman datasets show that the proposed models consistently outperform the baseline methods, including supervised and self-supervised ones. This reflects the proposed methods' strong representation learning and better generalization capabilities, especially in imbalanced multi-label classification, which

TABLE III: Hyperparameter settings.

Hyperparameter	Pre-training	Linear probing	Fine-tuning
- Backbone	ViT	ViT	ViT
- Learning rate	0.0012	0.001	0.001
- Batch size	128	64	64
- Epochs	800	100	100
- Optimizer	AdamW	AdamW	AdamW
- Learning rate scheduler	Consine anealing	-	Consine anealing
- Warump steps	40	-	5

is common in ECG signals. Among the proposed configurations, Scheme II often outperforms or is par with Scheme I on most metrics and datasets. While Scheme I still provides high and consistent performance, Scheme II tends to exploit deep representations more effectively. This trend is consistent across both the condition and rhythm tasks and across both large (PTB-XL) and smaller (Chapman) data scales, demonstrating the advantage of the PMA compared to PPA.

Out-of-distribution evaluation: We further evaluate the performance of our methods in the out-of-distribution setting, with two tasks built from the PTB-XL dataset: condition classification and rhythm classification. The corresponding results are presented in Tables VIII and IX. Table VIII presents the model performance in the out-of-distribution (OOD) scenario – a challenging scenario, but more closely reflects the practical applicability of the model. The results show that the proposed methods maintain high performance and exhibit superior generalization ability when faced with unseen data during training. In the linear probing setting, all three Schemes significantly outperform the baselines. In particular, Scheme II achieves the highest score in Sample AUC (97.25 ± 0.05), Macro F1 Score (24.83 ± 0.9), Macro mAP (32.44 ± 0.86), and Sample mAP (82.29 ± 0.18). Scheme III achieves comparable and highest results in metrics such as Macro AUC (93.08 ± 0.24), Instance Accuracy (35.43 ± 0.37), Sample Accuracy (97.89 ± 0.01) and Sample F1 Score (69.94 ± 0.18), demonstrating the stability of the representation learned through average pooling. In the fine-tuning setting, proposed schemes maintain the highest performance across the board, outperforming all supervised and self-supervised methods. Scheme III leads in Macro AUC (94.04 ± 0.29), Sample AUC (97.54 ± 0.05), Instance Accuracy (38.9 ± 0.63), Sample Accuracy (98.04 ± 0.02), and Sample F1 Score (73.08 ± 0.44). Meanwhile, Scheme II achieves the highest scores in Macro F1 Score (28.31 ± 0.97) and Sample F1 Score (35.19 ± 0.79), two important metrics reflecting the ability to discriminate rare pathological classes, which are often degraded in imbalanced datasets. Table IX provides the performance of the models for the rhythm classification problem in the context of OOD. The results show that SimCLR still performs well in sample metrics, while the proposed models show superiority for macro metrics. Overall, in the context of out-of-distribution (OOD) evaluation, the proposed models still maintain superior performance over the baseline methods on most evaluation metrics and classification tasks. Notably, Scheme III (IPASTMEM) shows a clear improvement over Scheme I (PPA), indicating that the rich representation synthesis

strategy offers a significant advantage in generalization ability in heterogeneous data scenarios.

Another observation is that although our proposed methods generally outperform SimCLR in various datasets and settings, the PTB-XL rhythm classification results show that SimCLR outperforms the proposed method in some metrics in fine-tuning. This phenomenon can be explained by the characteristics of the problem and the data. First, rhythm classification is a relatively simple task with only 11 classes, while the PTB-XL dataset is large enough to fine-tune the ResNet backbone effectively from pre-trained weights. In such a context, fine-tuning helps the ResNet in SimCLR adjust the weights and exploit the full power of the network architecture, thereby improving the performance, even surpassing the proposed methods in some cases. However, the linear probing section observation shows that SimCLR is far behind the proposed method, reflecting that the representation learned from SimCLR is not rich in information for the downstream task. SimCLR improves only with fine-tuning, mainly due to the ability to update all ResNet weights on a simple task with large enough data, rather than the inherent quality of pre-training. In contrast, in more complex settings, such as PTB-all condition classification, or on smaller datasets, such as Chapman, SimCLR significantly underperforms our proposed methods. Thus, this result confirms the limitations of SimCLR in learning general representations and reinforces the superiority of our proposed methods in maintaining stable performance across different contexts, especially complex tasks or limited data, which are more common in biomedical practice.

In summary, essential conclusions can be drawn from the above results.

- Across both evaluation scenarios, in-distribution and out-of-distribution, self-supervised learning methods show significant improvements over supervised learning methods on most evaluation metrics, classification tasks, and datasets.
- Fine-tuning strategies typically outperform linear probing in most cases, reflecting the ability to fine-tune the model representation as the entire parameter set is updated.
- Our proposed methods consistently outperform baselines - including self-supervised and supervised models - with stable and consistent performance across various datasets, classification tasks, and evaluation criteria.
- When applying pre-trained ViT to downstream classification tasks, combining information from multiple layers improves the representation quality, in which the PMA method outperforms PPA.

TABLE IV: PTB-XL condition results

Method	Model	PTB-XL condition							
		Macro AUC	Sample AUC	Instance Accuracy	Sample Accuracy	Macro F1 Score	Sample F1 Score	Macro mAP	Sample mAP
		Linear probing							
Self-supervised	SimCLR [40], [59]	84.97±0.28	94.63±0.31	29.37±1.47	97.45±0.02	12.43±0.62	61.88±0.84	18±0.6	73.6±0.51
	CPC [40]	89.97±0.3	96.04±0.09	32.6±0.39	97.66±0.01	17.12±0.69	66.23±0.2	22.85±0.94	77.79±0.17
	STMEM [35]	92.6±0.17	96.92±0.07	34.78±0.6	97.82 ±/−0.01	21.6±0.9	68.41±0.35	28.79±1.14	81.07±0.23
Proposed method	Scheme I - PPA	93.39±0.29	97.21±0.09	35.42±0.41	97.88±0.02	24.43±1.41	69.82±0.37	31.85±1.25	82.14±0.24
	Scheme II - PMA	93.44±0.14	97.22±0.08	35.57±0.34	97.89±0.02	24.73±0.78	69.93±0.31	32.25±0.6	82.28±0.12
	Scheme III - IPASTMEM	93.2±0.3	97.14±0.09	35.74±0.42	97.89±0.02	23.53±1.11	69.93±0.33	31.58±1.58	82.02±0.25
		Fine-tuning							
Supervised	XResnet1d50 [8], [40]	90.46±0.38	96.36±0.13	34.96±1.13	97.79±0.03	21.83±0.86	68.94±0.65	28.19±0.5	79.72±0.56
	ViT1d [35], [58]	85.31±0.45	94.79±0.24	31.27±1.9	97.45±0.05	17.47±1.6	63.79±1.03	21.32±1.25	74.09±0.66
	4FC+2LSTM+2FC [40]	91.14±0.48	96.59±0.25	35.62±0.93	97.8±0.06	23.9±1.32	69.65±0.8	29.31±1.05	80.11±0.69
Self-supervised	SimCLR [40], [59]	92.41±0.51	96.86±0.18	35.34±1.43	97.84±0.06	24.31±1.23	70.28±0.65	31.1±0.91	80.95±0.68
	CPC [40]	91.24±0.36	96.52±0.09	34.61±0.22	97.77±0.02	19.62±0.69	68.26±0.26	25.92±0.76	79.61±0.32
	STMEM [35]	93.69±0.28	97.41±0.1	38.26±1.06	98.02±0.03	26.21±1.43	72.4±0.6	33.01±1.35	83.53±0.35
Proposed method	Scheme I - PPA	94.01±0.26	97.55±0.06	38.66±0.56	98.03±0.02	27.65±0.85	72.85±0.36	34.33±0.87	83.9±0.21
	Scheme II - PMA	94.07±0.18	97.6±0.15	38.44±0.43	98.03±0.02	27.87±1.11	72.77±0.28	34.8±0.75	83.94±0.24
	Scheme III - IPASTMEM	93.89±0.2	97.44±0.17	38.88±0.8	98.03±0.04	26.79±1.1	72.79±0.62	33.79±0.94	83.61±0.53

TABLE V: PTB-XL rhythm results

Method	Model	PTB-XL rhythm							
		Macro AUC	Sample AUC	Instance Accuracy	Sample Accuracy	Macro F1 Score	Sample F1 Score	Macro mAP	Sample mAP
		Linear probing							
Self-supervised	SimCLR [40], [59]	87.12±0.28	96.28±0.48	81.8±0.36	97.43±0.04	25.82±1.39	83.77±0.63	32.42±1.96	89.18±0.79
	CPC [40]	91.51±0.37	94.33±0.17	82.05±0.23	97.74±0.03	30.69±2.58	82.25±0.27	33.43±3.75	86.21±0.34
	STMEM [35]	97.25±0.21	95.33±0.12	85.55±0.38	98.24±0.05	44.1±2.73	85.72±0.28	51.08±3.3	88.76±0.22
Proposed method	Scheme I - PPA	97.18±0.16	95.5±0.12	86.02±0.24	98.3±0.03	46.79±2.73	86.28±0.24	55.33±2.68	89.18±0.23
	Scheme II - PMA	97.14±0.24	95.68±0.11	86.27±0.26	98.32±0.04	48.21±4.17	86.6±0.15	55.18±3.55	89.49±0.14
	Scheme III - IPASTMEM	96.66±0.16	95.7±0.12	86.34±0.28	98.31±0.03	47.46±2.24	86.61±0.25	55.36±2.32	89.54±0.23
		Fine-tuning							
Supervised	XResnet1d50 [8], [40]	90.13±3.12	94.75±0.39	84.47±0.46	98.1±0.06	40.9±2.7	84.68±0.54	45.79±2.8	87.74±0.68
	ViT1d [35], [58]	88.37±0.81	93.14±0.66	78.9±0.96	97.28±0.09	32.52±3.43	78.94±1.05	35.66±3.01	83.56±1.21
	4FC+2LSTM+2FC [40]	93.94±3	91.72±7.84	78.6±14.07	97.59±1.12	37.4±8.93	78.43±14.87	43.6±6.32	81.62±15.34
Self-supervised	SimCLR [40], [59]	96.27±0.6	97.32±0.49	89.05±0.78	98.53±0.08	44.88±2.48	89.89±0.96	50.94±2.05	92.84±0.93
	CPC [40]	92.98±0.74	94.58±0.14	83.21±0.23	97.91±0.04	36.5±2.34	83.29±0.23	39.88±2.52	86.9±0.25
	STMEM [35]	97.04±0.26	95.51±0.17	86.47±0.3	98.36±0.04	47.87±2.58	86.57±0.35	54.46±2.16	89.33±0.32
Proposed method	Scheme I - PPA	96.88±0.2	95.64±0.23	86.79±0.31	98.4±0.04	48.51±2.45	86.9±0.37	55.97±2.59	89.61±0.4
	Scheme II - PMA	96.74±0.41	95.76±0.17	86.67±0.33	98.38±0.05	50.9±2.73	87.03±0.4	56.64±2.78	89.79±0.34
	Scheme III - IPASTMEM	96.36±0.45	95.62±0.21	86.74±0.4	98.37±0.06	48.34±3.49	86.8±0.44	54.49±4.26	89.55±0.39

TABLE VI: Chapman condition results

Method	Model	Chapman condition							
		Macro AUC	Sample AUC	Instance Accuracy	Sample Accuracy	Macro F1 Score	Sample F1 Score	Macro mAP	Sample mAP
		Linear probing							
Self-supervised	SimCLR [40], [59]	77.37±0.35	89.44±0.62	36.35±0.72	98.17±0.02	12.52±0.95	57.81±0.95	16.91±0.68	67.89±1.02
	CPC [40]	81.96±0.48	95.19±0.26	47.28±0.63	98.51±0.02	14.87±0.68	70.4±0.47	19.72±0.76	81.32±0.52
	STMEM [35]	85.24±0.22	97.76±0.24	53.58±0.66	98.77±0.01	19.76±1.12	78.5±0.52	24.88±1.03	88.96±0.43
Proposed method	Scheme I - PPA	85.63±0.28	98.16±0.19	55.41±0.54	98.85±0.01	21.45±0.45	80.19±0.3	26.55±0.71	90.41±0.22
	Scheme II - PMA	85.69±0.3	98.18±0.23	55.43±0.38	98.85±0.01	21.29±0.52	80.25±0.38	26.43±0.59	90.44±0.4
	Scheme III - IPASTMEM	85.72±0.3	97.91±0.25	54.4±0.66	98.82±0.02	20.72±1.3	79.29±0.61	26.11±1.16	89.63±0.53
		Fine-tuning							
Supervised	XResnet1d50 [8], [40]	82.97±0.87	96.68±0.58	49.54±1.55	98.62±0.04	19.44±1.56	75.25±1.17	23.94±1.19	85.56±1.08
	ViT1d [35], [58]	76.97±0.7	93.78±1.35	42.13±1.72	98.22±0.06	12.85±1.04	64.69±2.3	16.26±0.52	75.21±2.45
	4FC+2LSTM+2FC [40]	82.67±2.17	95.63±3.86	45.71±14.66	98.28±1.07	19.2±4.64	70.5±14.86	23.9±4.44	81.09±14.72
Self-supervised	SimCLR [40], [59]	83.65±0.44	97.7±0.47	54.47±2.34	98.79±0.08	22.59±1.62	79.38±1.09	27.4±1.41	88.8±0.88
	CPC [40]	82.69±0.34	96.13±0.31	49.85±0.61	98.61±0.03	16.56±0.61	73.37±0.5	22.27±0.89	84.03±0.58
	STMEM [35]	85.37±0.25	98.22±0.23	55.42±1.02	98.84±0.03	21.82±0.95	80.39±0.77	27.09±0.77	90.38±0.61
Proposed method	Scheme I - PPA	85.72±0.27	98.25±0.19	56.05±0.59	98.87±0.01	22.8±0.49	80.95±0.46	27.91±0.56	90.73±0.38
	Scheme II - PMA	85.76±0.27	98.16±0.3	55.84±0.97	98.87±0.03	22.97±0.92	80.65±0.84	28.11±0.91	90.54±0.75
	Scheme III - IPASTMEM	85.84±0.22	98.02±0.37	55.09±0.9	98.84±0.03	22.31±1.39	79.97±0.87	27.61±1.35	89.98±0.81

TABLE VII: Chapman rhythm results

Method	Model	Chapman rhythm							
		Macro AUC	Sample AUC	Instance Accuracy	Sample Accuracy	Macro F1 Score	Sample F1 Score	Macro mAP	Sample mAP
		Linear probing							
Self-supervised	SimCLR [40], [59]	83.31±0.24	86.64±0.59	61.96±1.24	95.55±0.09	37.28±1.52	64.88±1.07	43.9±1.62	70.17 ±1.14
	CPC [40]	91.47±0.36	94.03±0.62	80.18±1.25	97.32±0.11	45.81±0.7	81.2±1.12	50.78±0.4	85.43±1.24
	STMEM [35]	94.42±0.07	97.6±0.16	90.44±0.47	98.67±0.06	57.99±0.88	91.16±0.29	62.43±0.48	93.67±0.33
Proposed method	Scheme I - PPA	94.68±0.1	97.85±0.22	91.79±0.58	98.85±0.06	59.19±1.19	92.23±0.39	64.25±0.47	94.4±0.41
	Scheme II - PMA	94.65±0.07	97.88±0.22	91.71±0.55	98.84±0.06	59.33±1.12	92.24±0.42	64.34±0.39	94.45±0.41
	Scheme III - IPASTMEM	94.67±0.11	97.82±0.23	91.51±0.39	98.8±0.04	58.77±0.76	91.89±0.45	63.47±1.22	94.2±0.46
		Fine-tuning							
Supervised	XResnet1d50 [8], [40]	91.94±1.5	96.06±0.62	86.95±1.71	98.22±0.18	52.8±1.63	87.75±1.41	56.93±1.61	90.57±1.3
	ViT1d [35], [58]	88.26±2.78	92.77±0.61	75.6±1.48	96.44±0.2	40.12±2.11	76.36±1.39	44.77±1.15	82.3±1.29
	4FC+2LSTM+2FC [40]	92.96±1.25	97.08±0.53	88.17±1.85	98.26±0.24	56.37±1.7	88.81±1.66	61.58±1.17	92.17±1.26
Self-supervised	SimCLR [40], [59]	93.87±0.8	97.1±0.73	89.35±1.28	98.51±0.15	55.75±2.42	89.97±1.43	61.57±2.2	92.57±1.44
	CPC [40]	92.39±0.73	95.31±0.31	84.04±0.75	97.78±0.13	47.96±1.22	84.66±0.8	52.89±0.86	88.36±0.64
	STMEM [35]	94.4±0.13	97.9±0.24	91.35±1.02	98.75±0.14	59.04±1.76	91.86±0.87	63.81±1.1	94.32±0.62
Proposed method	Scheme I - PPA	94.65±0.09	97.87±0.3	91.38±1.13	98.78±0.15	60.08±0.62	91.96±0.94	64.67±0.33	94.32±0.73
	Scheme II - PMA	94.61±0.12	97.93±0.29	91.72±0.68	98.81±0.08	60.33±2.17	92.18±0.6	64.74±1.74	94.49±0.58
	Scheme III - IPASTMEM	94.57±0.1	97.89±0.36	91.18±0.96	98.73±0.15	61±3.24	91.82±0.99	64.75±1.99	94.31±0.77

- Comparing the two pretrained strategies, STMEM and IPASTMEM, shows that integrating layers in the encoder of ViT significantly improves the model's efficiency on out-of-distribution datasets.

VII. CONCLUSION

In this study, we comprehensively analyzed the impact of each layer within the pretrained ViT on ECG signals. We demonstrated that relying solely on the last layer, common in practice, does not provide optimal performance. Through experiments on various datasets, evaluation metrics, and downstream tasks, we observed a consistent pattern: the performance of the early layers is typically lowest, gradually increases and peaks in the middle layers, and then slightly decreases in the last layers. Based on this finding, we proposed three strategies for exploiting multilayer representations, including (i) Post-pretraining Pooling-based Aggregation (PPA), (ii) Post-pretraining Mixture-of-layers Aggregation (PMA), and (iii) In-pretraining Pooling-based Aggregation STMEM (IPASTMEM) to enhance the quality of the base representation. Experimental results demonstrate that all three methods improve generalization and deliver superior performance, especially in non-distributional data, thereby highlighting the potential of exploiting multi-layer information in pre-trained Transformer models for biomedical applications. We plan to extend our research to multimodal ECG-text problems to integrate medical knowledge into the ECG signal representation. This approach aims to improve the model's ability to understand physiological and pathological contexts, thereby enabling accurate recognition of labels that have not been previously trained using zero-shot learning on downstream tasks.

REFERENCES

- [1] A. Thivya, N. Malaya Kumar, D. Vijayalakshmi, and A. Archana, "Analysis of various techniques for ECG signal in healthcare, past, present, and future," *Biomedical Engineering Advances*, vol. 6, 2023.
- [2] S. Marko, J. Fran, and P. Sinisa, "A convolutional neural network based approach to QRS detection," in *International Symposium on Image and Signal Processing and Analysis*. IEEE, 2017.
- [3] P. Saman and R. Jonathan, "Electrocardiogram monitoring and interpretation: From traditional machine learning to deep learning, and their combination," in *2018 Computing in Cardiology Conference (CinC)*. IEEE, 2018.
- [4] H. Awani Y., R. Pranav, H. Masoumeh, T. Geoffrey H., B. Codie, T. Mintu P., and N. Andrew Y., "Cardiologist-level arrhythmia detection and classification in ambulatory electrocardiograms using a deep neural network," *Nature Medicine*, pp. 65–69, 2019.
- [5] R. Antonio H., R. Manoel Horta, P. Gabriela M. M., O. Derick M., G. Paulo R., C. Jessica A., F. Milton P. S., A. Carl R., M. Peter W., J. Wagner Meira, S. Thomas B., and R. Antonio Luiz P., "Automatic diagnosis of the 12-lead ecg using a deep neural network," *Nature Communications*, vol. 11, no. 1, 2020.
- [6] A. Zachi I., K. Suraj, L.-J. Francisco, M. Paul M., L. Dorothy J., S. Gaurav, P. Patricia A., E.-S. Maurice, N. Peter A., M. Thomas M., A. Samuel J., S. Christopher G., C. Rickey E., and F. Paul A., "Screening for cardiac contractile dysfunction using an artificial intelligence-enabled electrocardiogram," *Nature Medicine*, pp. 70–74, 2019.
- [7] K. Wei-Yin, K. C. Siontis, A. Zachi I., R. E. Carter, K. Suraj, O. Steve R., D. Steven J., A. Michael J., G. Bernard J., A. M. Arruda-Olson, G. Jeffrey B., A. Samuel J., L.-J. Francisco, N. Rick A., and F. Paul A., "Detection of hypertrophic cardiomyopathy using a convolutional neural network-enabled electrocardiogram," *Journal of the American College of Cardiology*, vol. 75, no. 7, pp. 722–733, 2020.
- [8] S. Nils, W. Patrick, S. Tobias, and S. Wojciech, "Deep learning for ECG analysis: Benchmarks and insights from PTB-XL," *IEEE Journal of Biomedical and Health Informatics*, vol. 25, no. 5, p. 1519–1528, 2021.
- [9] M. Junaid, D. Ozer, Can, K. Serkan, I. Turker, and G. Moncef, "Real-time patient-specific ECG classification by 1D self-operational neural networks," *IEEE Transactions on Biomedical Engineering*, vol. 69, no. 5, pp. 1788–1801, 2022.
- [10] Z. Muhammad, Uzair, K. Serkan, and G. Moncef, "Global ECG classification by self-operational neural networks with feature injection," *IEEE Transactions on Biomedical Engineering*, vol. 70, no. 1, pp. 205 – 215, 2023.
- [11] L. Kiem H., P. H. Hieu, N. Thao B. T., N. Tu A., T. Tien N., and D. D. Cuong, "Lightx3ecg: A lightweight and explainable deep learning system for 3-lead electrocardiogram classification," *Biomedical Signal Processing and Control*, vol. 85, 2023.
- [12] H. Shengnan, X. Hang, J. Hongyu, W. Zhiwu, Z. Li, and J. Zhanlin, "G2-resnext: A novel model for ECG signal classification," *IEEE Access*, vol. 11, pp. 34 808 – 34 820, 2023.
- [13] P. Allam Jaya, P. Kiran Kumar, S. Samantray, S. Pradipta, K. P. Lalitha, and G. Tummalapalli, "A new approach of transparent and explainable ar-

TABLE VIII: PTB-XL condition results (out-of-distribution evaluation)

Method	Model	PTB-XL condition							
		Macro AUC	Sample AUC	Instance Accuracy	Sample Accuracy	Macro F1 Score	Sample F1 Score	Macro mAP	Sample mAP
		Linear probing							
Self-supervised	SimCLR [40], [59]	84.65±0.19	94.69±0.22	28.89±1.13	97.47±0.01	13.96±0.69	62.34±0.31	19.01±0.63	73.64±0.34
	CPC [40]	89.7±0.44	95.91±0.15	31.93±0.25	97.62±0.01	15.88±0.94	65.3±0.39	22.35±1.25	77.36±0.32
	STMEM [35]	92.17±0.18	96.89±0.12	34.18±0.36	97.79±0.01	21.68±1.32	68.14±0.31	29.41±1.16	80.98±0.19
Proposed method	Scheme I - PPA	92.73±0.34	97.21±0.08	35.26±0.45	97.88±0.02	24.77±0.71	69.64±0.32	32.3±0.66	82.2±0.17
	Scheme II - PMA	92.77±0.27	97.25±0.05	35.16±0.43	97.87±0.01	24.83±0.9	69.72±0.25	32.44±0.86	82.29±0.18
	Scheme III - IPASTMEM	93.08±0.24	97.2±0.09	35.43±0.37	97.89±0.01	24.32±1.16	69.94±0.18	31.81±1.07	82.18±0.15
		Fine-tuning							
Supervised	XResnet1d50 [8], [40]	90.46±0.38	96.36±0.13	34.96±1.13	97.79±0.03	21.83±0.86	68.94±0.65	28.19±0.5	79.72±0.56
	ViT1d [35], [58]	85.31±0.45	94.79±0.24	31.27±1.9	97.45±0.05	17.47±1.6	63.79±1.03	21.32±1.25	74.09±0.66
	4FC+2LSTM+2FC [40]	91.14±0.48	96.59±0.25	35.62±0.93	97.8±0.06	23.9±1.32	69.65±0.8	29.31±1.05	80.11±0.69
Self-supervised	SimCLR [40], [59]	92.38±0.42	96.96±0.19	34.75±1.51	97.85±0.04	24.51±2.13	70.43±0.73	30.95±1.51	81.24±0.63
	CPC [40]	90.64±0.27	96.35±0.07	33.8±0.31	97.74±0.01	19.33±0.39	67.75±0.22	26.4±0.48	79.05±0.15
	STMEM [35]	93.56±0.29	97.43±0.09	38.23±0.75	98.02±0.01	27.01±1.06	72.57±0.43	33.44±1.32	83.55±0.29
Proposed method	Scheme I - PPA	93.82±0.22	97.48±0.12	38.22±0.81	98.02±0.02	27.97±0.55	72.6±0.39	34.34±0.8	83.6±0.35
	Scheme II - PMA	93.92±0.12	97.47±0.12	38.38±0.59	98.01±0.03	28.31±0.97	72.52±0.4	35.19±0.79	83.56±0.43
	Scheme III - IPASTMEM	94.04±0.29	97.54±0.05	38.9±0.63	98.04±0.02	27.79±1.44	73.08±0.44	34.87±1.53	83.97±0.19

TABLE IX: PTB-XL rhythm results (out-of-distribution evaluation)

Method	Model	PTB-XL rhythm							
		Macro AUC	Sample AUC	Instance Accuracy	Sample Accuracy	Macro F1 Score	Sample F1 Score	Macro mAP	Sample mAP
		Linear probing							
Self-supervised	SimCLR [40], [59]	84.98±0.71	96.17±0.36	81.38±0.6	97.36±0.05	24.42±0.87	83.32±0.43	28.84±0.45	88.75±0.61
	CPC [40]	90.42±0.81	94.25±0.11	81.28±0.4	97.59±0.05	32.21±3.04	81.54±0.32	36.41±2.97	85.89±0.26
	STMEM [35]	96.79±0.32	95.47±0.11	85.78±0.16	98.24±0.04	46.33±4.18	85.98±0.23	53.56±4.03	89.02±0.19
Proposed method	Scheme I - PPA	96.59±0.18	95.57±0.18	86.28±0.29	98.34±0.04	50.55±3.26	86.64±0.35	57.07±2.54	89.4±0.35
	Scheme II - PMA	96.54±0.23	95.53±0.13	86.22±0.19	98.33±0.03	50.5±2.78	86.53±0.26	56.71±2.89	89.34±0.26
	Scheme III - IPASTMEM	97.02±0.3	95.63±0.14	86.27±0.24	98.32±0.03	49.65±3.34	86.5±0.23	55.16±2.93	89.4±0.25
		Fine-tuning							
Supervised	XResnet1d50 [8], [40]	90.13±3.12	94.75±0.39	84.47±0.46	98.1±0.06	40.9±2.7	84.68±0.54	45.79±2.8	87.74±0.68
	ViT1d [35], [58]	88.36±0.81	93.17±0.66	78.86±0.95	97.28±0.09	32.59±3.39	78.9±1.05	35.93±2.85	83.55 ± 1.21
	4FC+2LSTM+2FC [40]	93.94±3	91.72±7.84	78.6±14.07	97.59±1.12	37.4±8.93	78.43±14.87	43.6±6.32	81.62±15.34
Self-supervised	SimCLR [40], [59]	96.44±0.45	97.41±0.43	89.09 ± 0.73	98.54±0.09	44.28±2.87	90.06±0.82	51.53±3.23	93.01±0.83
	CPC [40]	92.11±1.37	94.4±0.07	82.22±0.24	97.73±0.05	33.89±2.37	82.37±0.16	39.18±2.74	86.41±0.09
	STMEM [35]	96.83±0.28	95.51±0.2	86.49±0.35	98.38±0.03	49.44±3.26	86.69±0.35	54.8±3.45	89.36±0.39
Proposed method	Scheme I - PPA	96.55±0.3	95.59±0.26	86.51±0.34	98.38±0.05	50.43±2.89	86.79±0.43	55.68±2.73	89.49±0.46
	Scheme II - PMA	96.08±0.38	95.72±0.18	86.85±0.27	98.4±0.03	49.01±2.98	87.1±0.28	54.76±2.89	89.81±0.33
	Scheme III - IPASTMEM	96.73±0.42	95.56±0.23	86.36±0.45	98.35±0.05	49.92±3.19	86.58±0.36	54.96±3.41	89.38±0.39

- tificial intelligence technique for patient-specific ECG beat classification,” *IEEE Sensors Letters*, vol. 7, no. 5, 2023.
- [14] Y. Shunxiang, L. Cheng, Z. Zhigang, X. Bingrong, Z. Junbin, and Z. Zhi-dong, “A multi-view multi-scale neural network for multi-label ECG classification,” *IEEE Transactions on Emerging Topics in Computational Intelligence*, vol. 7, no. 3, 2023.
- [15] X. Pan, Z. Hao, Y. Yicheng, X. Lrui, B. Zhongrui, and C. Xianxiang, “Spatiotemporal 3-D variations modeling with self-attention for multilabel ECG classification,” *IEEE Sensors Journal*, vol. 24, no. 11, pp. 18 710 – 18 724, 2024.
- [16] H. Wei, W. Ning, F. Panpan, W. Haiyan, W. Zongmin, and Z. Bing, “A multi-resolution mutual learning network for multi-label ECG classification,” in *International Conference on Bioinformatics and Biomedicine (BIBM)*. IEEE, 2024.
- [17] Z. Muhammad, W. Sungpil, L. Sunhwan, and K. Daeyoung, “Deep representation learning with sample generation and augmented attention module for imbalanced ECG classification,” *IEEE Journal of Biomedical and Health Informatics*, vol. 28, no. 5, pp. 2461 – 2472, 2024.
- [18] L. Yang, W. Guijin, X. Zhouhui, Y. Wenming, and S. Li, “A dual-scale lead-separated transformer for ECG classification,” in *Annual International Conference of the IEEE Engineering in Medicine & Biology Society (EMBC)*. IEEE, 2023.
- [19] E.-G. Hany and E. Emadeldeen, “ECGTransForm: Empowering adaptive ECG arrhythmia classification framework with bidirectional transformer,” *Biomedical Signal Processing and Control*, vol. 89, 2024.
- [20] T. Xiaoya, B. Jake, S. Benjamin A., and T. Tolga, “Hierarchical transformer for electrocardiogram diagnosis,” *arXiv:2411.00755*, 2024.
- [21] D. S. Lakhan and K. S. Ramesh, “Detection and delineation of the enigmatic U-wave in an electrocardiogram,” *International Journal of Information Technology*, vol. 13, p. 2525–2532, 2021.
- [22] L. Xiaoyu, L. Chen, W. Yuhua, S. Yuyao, W. Jishang, and L. Xiang, “BaT: Beat-aligned transformer for electrocardiogram classification,” in *International Conference on Data Mining (ICDM)*. IEEE, 2021.
- [23] G. Bryan, H. Ryan, R. Gautham, N. Andrew, T. Geoff, and R. Pranav, “3KG: Contrastive learning of 12-lead electrocardiograms using physiologically-inspired augmentations,” in *Neural Information Processing Systems (NeurIPS)*. PMLR, 2021.
- [24] K. Dani, Z. Tingting, and C. David A., “CLOCs: Contrastive learning of cardiac signals across space, time, and patients,” in *International Conference on Machine Learning (ICML)*. PMLR, 2021.
- [25] S. Sahar, E. Ali, and H. Javad, “Analysis of augmentations for contrastive ECG representation learning,” in *2022 International Joint Conference on Neural Networks (IJCNN)*, 2022.
- [26] W. Crystal T., H. Ming-En, L. Chien-Liang, and T. Vincent S., “Contrastive heartbeats: Contrastive learning for self-supervised ECG represen-

- tation and phenotyping,” in *IEEE International Conference on Acoustics, Speech and Signal Processing (ICASSP)*. IEEE, 2022.
- [27] S. Pritam and E. Ali, “Self-supervised ECG representation learning for emotion recognition,” *IEEE Transactions on Affective Computing*, vol. 13, no. 3, pp. 1541 – 1554, 2022.
 - [28] L. Duc, T. Sang, B. Patel, A. Donald A., and L. Ngan, “sCL-ST: Supervised contrastive learning with semantic transformations for multiple lead ECG arrhythmia classification,” *IEEE Journal of Biomedical and Health Informatics*, vol. 27, no. 6, pp. 2818 – 2828, 2024.
 - [29] W. Ning, F. Panpan, G. Zhaoyang, Z. Yanjie, Z. Bing, and W. Zongmin, “Adversarial spatiotemporal contrastive learning for electrocardiogram signals,” *IEEE Transactions on Neural Networks and Learning Systems*, vol. 35, no. 10, pp. 13 845 – 13 859, 2024.
 - [30] Z. Huaicheng, L. Wenhan, S. Jiguang, C. Sheng, W. Hao, and H. Jin, “MacFE: Masked autoencoders family of electrocardiogram for self-supervised pretraining and transfer learning,” *IEEE Transactions on Instrumentation and Measurement*, vol. 72, 2022.
 - [31] Z. Wenrui, Y. Ling, G. Shijia, and H. Shenda, “Self-supervised time series representation learning via cross reconstruction transformer,” *IEEE Transactions on Neural Networks and Learning Systems*, vol. 35, no. 11, pp. 16 129 – 16 138, 2024.
 - [32] Z. Ya, D. Xiaolin, H. Yanni, L. Yang, F. Xiaohan, and Z. Wei, “Masked transformer for electrocardiogram classification,” *arXiv preprint arXiv:2309.07136*, 2024.
 - [33] W. Kuba and C. Tim O. F., “Self-supervised pre-training with joint-embedding predictive architecture boosts ECG classification performance,” *arXiv preprint arXiv:2410.13867*, 2024.
 - [34] K. Seun, “Learning general representation of 12-lead electrocardiogram with a joint-embedding predictive architecture,” *arXiv preprint arXiv:2410.08559*, 2024.
 - [35] N. Yeongyeon, P. Minje, T. Yunwon, and J. Sunghoon, “Guiding masked representation learning to capture spatio-temporal relationship of electrocardiogram,” in *International Conference on Learning Representations (ICLR)*. PMLR, 2024.
 - [36] L. Xiang, Y. Hanshu, H. Shenda, and F. Mengling, “Towards enhancing time series contrastive learning: A dynamic bad pair mining approach,” in *International Conference on Machine Learning (ICML)*. PMLR, 2024.
 - [37] L. Che, W. Zhongwei, O. Cheng, S. Anand, B. Wenjia, and A. Rossella, “Zero-shot ECG classification with multimodal learning and test-time clinical knowledge enhancement,” in *International Conference on Machine Learning (ICML)*. PMLR, 2024.
 - [38] H. Kaiming, C. Xinlei, X. Saining, L. Yanghao, D. Piotr, and G. Ross, “Masked autoencoders are scalable vision learners,” in *IEEE/CVF Conference on Computer Vision and Pattern Recognition (CVPR)*. IEEE, 2022.
 - [39] L. Jun, L. Che, C. Sibo, A. Rossella, and H. Shenda, “Frozen language model helps ECG zero-shot learning,” *arXiv preprint arXiv:2303.12311*, 2023.
 - [40] M. Temesgen and S. Nils, “Self-supervised representation learning from 12-lead ECG data,” *Computers in Biology and Medicine*, vol. 141, 2022.
 - [41] O. Aaron van den, L. Yazhe, and V. Oriol, “Representation learning with contrastive predictive coding,” *arXiv preprint arXiv:1807.03748*, 2019.
 - [42] R. Maithra, U. Thomas, K. Simon, Z. Chiyuan, and D. Alexey, “Do vision transformers see like convolutional neural networks?” in *Neural Information Processing Systems (NeurIPS)*. PMLR, 2021.
 - [43] M. Shentong, S. Zhun, and L. Chao, “Multi-level contrastive learning for self-supervised vision transformers,” in *IEEE/CVF Conference on Computer Vision and Pattern Recognition (CVPR)*. IEEE, 2023.
 - [44] G. Jun, H. Di, T. Xu, Q. Tao, W. Liwei, and L. Tie-Yan, “Representation degeneration problem in training natural language generation models,” in *International Conference on Learning Representations (ICLR)*. PMLR, 2019.
 - [45] S. Oscar, A. Md Rifat, Z. Dan, P. Niket, N. Jalal, L. Yann, and S.-Z. Ravid, “Layer by layer: Uncovering hidden representations in language models,” *arXiv preprint arXiv:2502.02013*, 2025.
 - [46] W. Peihao, Z. Wenqing, C. Tianlong, and W. Zhangyang, “Anti-oversmoothing in deep vision transformers via the fourier domain analysis: From theory to practice,” in *International Conference on Learning Representations (ICLR)*. PMLR, 2022.
 - [47] N. Tam, N. Tan M., and B. Richard G., “Mitigating over-smoothing in transformers via regularized nonlocal functionals,” in *Neural Information Processing Systems (NeurIPS)*. PMLR, 2023.
 - [48] G. Yuan, K. Sameer, K. Leonid, and G. James, “Whisper-AT: Noise-robust automatic speech recognizers are also strong general audio event taggers,” in *Interspeech*, 2023.
 - [49] T. Cheng-Hao, M. Zheda, and C. Wei-Lun, “Visual query tuning: Towards effective usage of intermediate representations for parameter and memory efficient transfer learning,” in *IEEE/CVF Conference on Computer Vision and Pattern Recognition (CVPR)*. IEEE, 2023.
 - [50] V. Martina G., S. Timothy, and R. Gemma, “Analyzing vision transformers for image classification in class embedding space,” in *Neural Information Processing Systems (NeurIPS)*. PMLR, 2023.
 - [51] Y. Jinsu, K. Taehoon, L. Sihaeng, K. Seung Hwan, L. Honglak, and K. Tae Hyun, “Enriched CNN-Transformer feature aggregation networks for super-resolution,” in *IEEE/CVF Conference on Computer Vision and Pattern Recognition (CVPR)*. IEEE, 2023.
 - [52] C. Zixiang, D. Yihe, W. Yue, G. Quanquan, and L. Yuanzhi, “Towards understanding mixture of experts in deep learning,” *arXiv:2208.02813*, 2022.
 - [53] C. Weilin, J. Juyong, W. Fan, T. Jing, K. Sunghun, and H. Jiayi, “A survey on mixture of experts in large language models,” *arXiv:2407.06204*, 2024.
 - [54] A. Erick Andres Perez, G. Annie, S. Amit, L. Chengyu, S. Ashish, S. Salman, R. Ali Bahrami, R. Matthew, and C. Gari, “Classification of 12-lead ECGs: The physionet/computing in cardiology challenge 2020,” *Physiological Measurement*, vol. 41, no. 12, p. 124003, 2021.
 - [55] Z. Jianwei, Z. Jianming, D. Sidy, Y. Hai, G. Hangyuan, and R. Cyril, “A 12-lead electrocardiogram database for arrhythmia research covering more than 10, 000 patients,” *Scientific Data*, vol. 7, no. 1, 2020.
 - [56] A. H. Ribeiro, G. M. Paixao, E. M. Lima, M. Horta Ribeiro, M. M. Pinto Filho, P. R. Gomes, D. M. Oliveira, W. Meira Jr, T. B. Schon, and A. L. P. Ribeiro, “Code-15%: a large scale annotated dataset of 12-lead ECGs,” *Zenodo*, 2021.
 - [57] W. Patrick, S. Nils, B. Ralf-Dieter, K. Dieter, L. Fatima I., S. Wojciech, and S. Tobias, “PTB-XL, a large publicly available electrocardiography dataset,” *Scientific Data*, vol. 7, no. 1, 2020.
 - [58] D. Alexey, B. Lucas, K. Alexander, W. Dirk, Z. Xiaohua, U. Thomas, D. Mostafa, M. Matthias, H. Georg, G. Sylvain, U. Jakob, and H. Neil, “An image is worth 16x16 words: Transformers for image recognition at scale,” in *International Conference on Learning Representations (ICLR)*. PMLR, 2021.
 - [59] C. Ting, K. Simon, N. Mohammad, and H. Geoffrey, “A simple framework for contrastive learning of visual representations,” in *International Conference on Machine Learning (ICML)*. PMLR, 2020.
 - [60] G. Guy and O. Stanley, “Nonlocal linear image regularization and supervised segmentation,” *Multiscale Modeling & Simulation*, vol. 6, 2007.
 - [61] G. Guy and O. Stanley, “Nonlocal operators with applications to image processing,” *Multiscale Modeling & Simulation*, vol. 7, 2009.

APPENDIX

APPENDIX A: MATHEMATICAL ANALYSIS

We conduct a mathematical analysis to explain the information transformation process through the layers of the Transformer model trained by the masked modeling mechanism. To understand the depth-based representational characteristics of the model, we examine the average cosine similarity between patch embeddings at each layer of the Transformer encoder. The analysis results show a remarkable trend: "the average cosine similarity increases gradually from the early layers, converges at the middle layers, and decreases at the last layers". This phenomenon suggests that the model gradually centralizes information in the middle stage, before redistributing or recoding at the later stages, reflecting a complex representational reorganization process as the network deepens. We denote

- $\mathbf{x} = [\mathbf{x}_1, \mathbf{x}_2, \dots, \mathbf{x}_N]$: ECG patch embeddings.
- \mathcal{M} : the set of masked patches.
- $\mathbf{h}_i^{(l)} \in \mathbb{R}^d$: i -th patch embedding at layer l -th, where $l = 1, \dots, L$.

We first define a non-local functional of weighted differences as in [47], [60], [61]

$$J(\mathbf{h}) = \frac{1}{2} \int_{\Omega} \int_{\Omega} \|\mathbf{h}(x) - \mathbf{h}(y)\|_2^2 K(x, y) dx dy, \quad (23)$$

where

- Ω : the space of patch embeddings,
- $K(x, y)$: the similarity between patch x and y .

The variation of $J(\mathbf{h})$ with respect to \mathbf{h} is calculated as

$$\delta J(\mathbf{h}) = \int_{\Omega} \int_{\Omega} \langle \mathbf{h}(x) - \mathbf{h}(y), \delta \mathbf{h}(x) - \delta \mathbf{h}(y) \rangle K(x, y) dx dy, \quad (24)$$

Due to the symmetry of $K(x, y)$, $\delta J(\mathbf{h})$ is rewritten

$$\begin{aligned} \delta J(\mathbf{h}) &= \int_{\Omega} \int_{\Omega} \langle \mathbf{h}(x) - \mathbf{h}(y), \delta \mathbf{h}(x) \rangle K(x, y) dx dy - \int_{\Omega} \int_{\Omega} \langle \mathbf{h}(x) - \mathbf{h}(y), \delta \mathbf{h}(y) \rangle K(x, y) dx dy \\ &= 2 \int_{\Omega} \int_{\Omega} \langle \mathbf{h}(x) - \mathbf{h}(y), \delta \mathbf{h}(x) \rangle K(x, y) dx dy \end{aligned} \quad (25)$$

Due to $\delta J(\mathbf{h}) = \int_{\Omega} \langle \nabla_{\mathbf{h}(x)} J(\mathbf{h}), \delta \mathbf{h}(x) \rangle dx$, follow (25) the gradient flow is as follows

$$\frac{\partial \mathbf{h}(x, t)}{\partial t} = -\nabla_{\mathbf{h}(x)} J(\mathbf{h}) = -2 \int_{\Omega} (\mathbf{h}(x) - \mathbf{h}(y)) K(x, y) dy. \quad (26)$$

We next discretize the gradient flow using the Euler method with $\nabla t = 1$

$$\begin{aligned} \mathbf{h}^{(k+1)}(x) &= \mathbf{h}^{(k)}(x) - \Delta t \cdot \nabla_{\mathbf{h}(x)} J(\mathbf{h}) = \mathbf{h}^{(k)}(x) - 2 \int_{\Omega} (\mathbf{h}^{(k)}(x) - \mathbf{h}^{(k)}(y)) K(x, y) dy. \\ &= \mathbf{h}^{(k)}(x) - 2 \mathbf{h}^{(k)}(x) \int_{\Omega} K(x, y) dy + 2 \int_{\Omega} \mathbf{h}^{(k)}(y) K(x, y) dy \\ &= u^{(k)}(x) \left(1 - 2 \int_{\Omega} K(x, y) dy \right) + 2 \int_{\Omega} u^{(k)}(y) K(x, y) dy. \end{aligned} \quad (27)$$

Let:

$$\Delta t(x) = \frac{1}{2 \int_{\Omega} K(x, y) dy}, \quad (28)$$

The update equation then simplifies to:

$$\mathbf{h}^{(k+1)}(x) = 2 \Delta t(x) \int_{\Omega} \mathbf{h}^{(k)}(y) K(x, y) dy = \frac{\int_{\Omega} \mathbf{h}^{(k)}(y) K(x, y) dy}{\int_{\Omega} K(x, y) dy} = \int_{\Omega} \mathbf{h}^{(k)}(y) \cdot \frac{K(x, y)}{\int_{\Omega} K(x, y') dy'} dy. \quad (29)$$

Approximate the integral using a weighted sum over sampled points y_j (corresponding to tokens)

$$\int_{\Omega} \mathbf{h}^{(k)}(y) \cdot \frac{K(x, y)}{\int_{\Omega} K(x, y') dy'} dy \approx \sum_{j=1}^N \mathbf{h}_j^{(k)} \cdot \frac{K(x, y_j)}{\sum_{j'=1}^N K(x, y_{j'})}. \quad (30)$$

The kernel $K(x, y_j)$ is typically defined using softmax attention:

$$K(x, y_j) = \exp \left(\frac{\mathbf{q}(x)^\top \mathbf{k}(y_j)}{\sqrt{D}} \right). \quad (31)$$

As a result:

$$\mathbf{h}_i^{(k+1)} = \frac{\sum_{j=1}^N \exp\left(\frac{\mathbf{q}_i^\top \mathbf{k}_j}{\sqrt{D}}\right) \mathbf{h}_j^{(k)}}{\sum_{j=1}^N \exp\left(\frac{\mathbf{q}_i^\top \mathbf{k}_j}{\sqrt{D}}\right)}. \quad (32)$$

This is precisely the self-attention formula in Transformers

$$\mathbf{h}_i^{(k+1)} = \sum_{j=1}^N \mathbf{A}_{ij} \mathbf{h}_j^{(k)}, \mathbf{A}_{ij} = \text{softmax}\left(\frac{\mathbf{q}_i^\top \mathbf{k}_j}{\sqrt{D}}\right). \quad (33)$$

This indicates that the self-attention mechanism in the Transformer architecture can be interpreted as a gradient descent update step that minimizes a non-local function $J(\mathbf{h})$. Optimizing this function means smoothing the input signals in a controlled manner through the weight function $K(x, y)$, thereby eliminating noise and improving generalization. [47] proved that when the model progresses through the deep layers, the embedding vectors corresponding to the patches tend to converge to the exact representation, called "over-smoothing". As a result, the cosine similarity between two patch embeddings converges to 1.

The above analysis has clarified that the mechanism leading to the increase of the average cosine similarity between tokens through each layer in Transformer models originates from the diffusion property of self-attention when optimizing the function $J(\mathbf{h})$. In the case of the pre-trained ViT trained by the masked modeling method with the MSE loss function to reconstruct the masked patches, the role of the MSE loss is equivalent to a fidelity constraint component in the overall optimization problem. Therefore, the training process can then be viewed as minimizing an energy function of the form

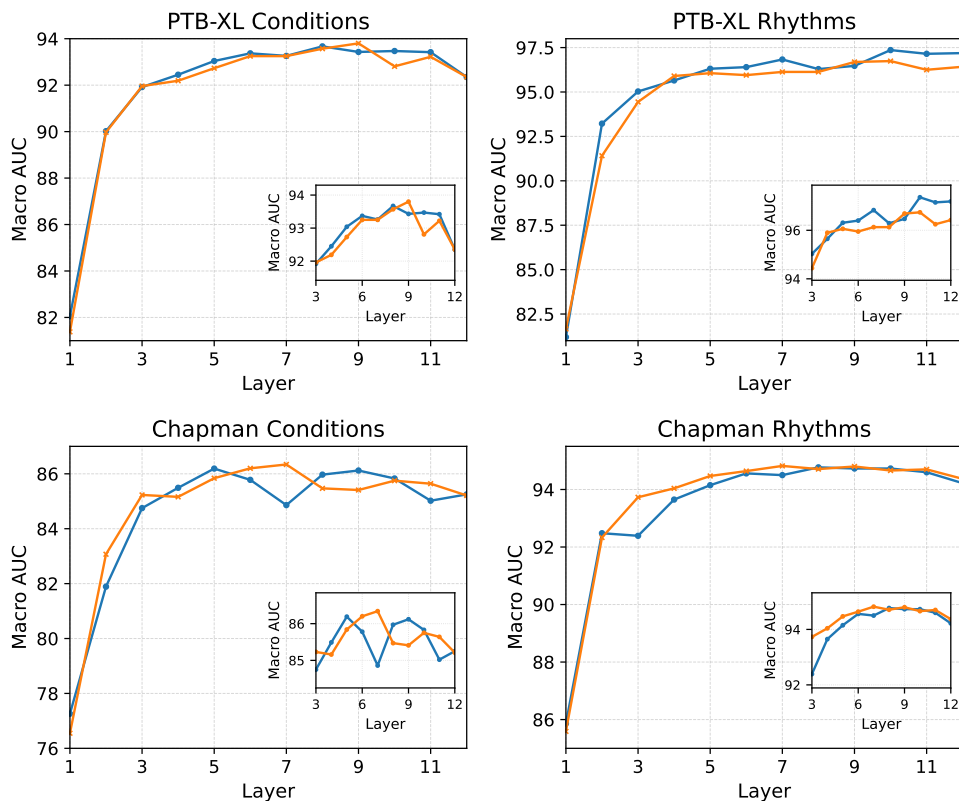
$$\mathcal{E} = J(\mathbf{h}) + \mathcal{L}_{\text{MSE}} = J(\mathbf{h}) + \frac{1}{|\mathcal{M}|} \sum_{i \in \mathcal{M}} \left\| f_{\text{dec}}(\mathbf{e}_i, \mathbf{h}^{(L)}) - \mathbf{x}_i \right\|^2, \quad (34)$$

where

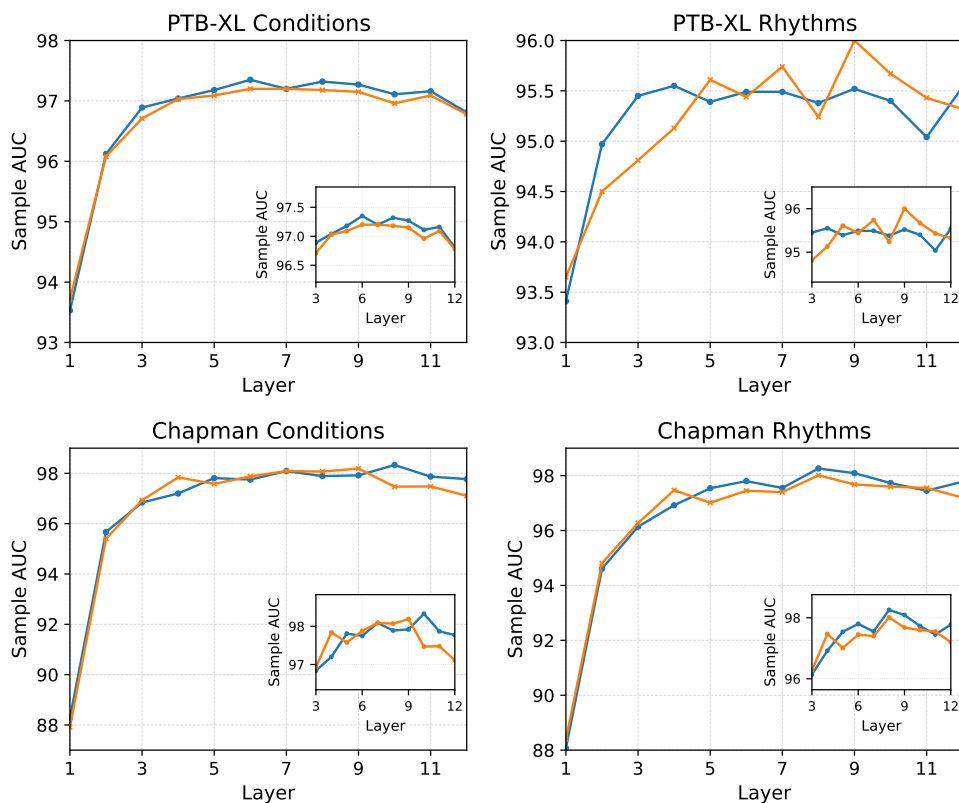
- $J(\mathbf{h})$ is a "smoothing" term, leading to increasing cosine similarity. Although the $J(\mathbf{h})$ is not explicitly expressed during the training of the masked ViT, as analyzed above, $J(\mathbf{h})$ is essentially equivalent to the self-attention mechanism. Therefore, $J(\mathbf{h})$ can be viewed as a latent component that plays a vital role in the structure and operation of the energy function \mathcal{E} .
- \mathbf{e}_i is random embeddings of masked patches.
- \mathcal{L}_{MSE} plays a role in maintaining fidelity to the original signal, forcing the model to preserve local information, which tends to reduce the similarity between patch embeddings.

APPENDIX B: HIDDEN LAYER ANALYSIS

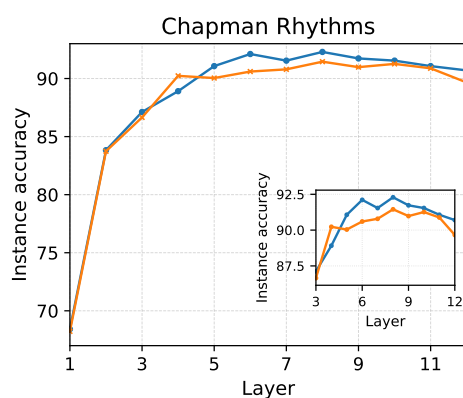
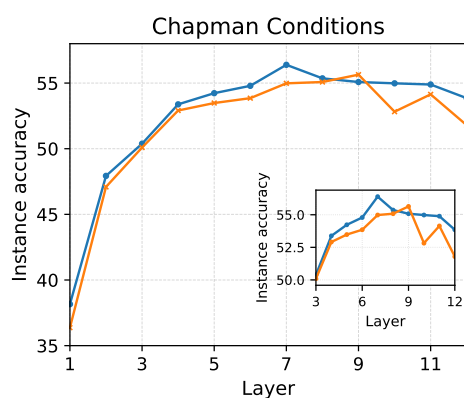
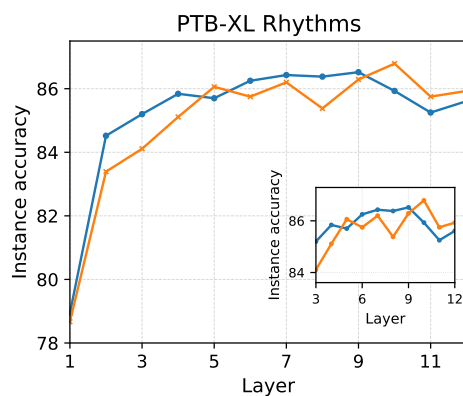
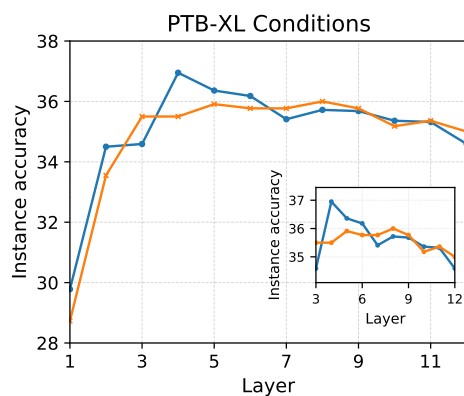
Figure 9 illustrates the classification performance of the STMEM and IPASTMEM models on each representation layer (from layer 1 to layer 12) on four datasets: PTB-XL Conditions, PTB-XL Rhythms, Chapman Conditions, and Chapman Rhythms. The plots show the macro AUC, sample AUC, instance precision, sample accuracy, macro F1 score, sample F1 score, macro mAP, and sample mAP (h) values when training the classifier on the representations extracted across layers in the pre-trained ViT model.



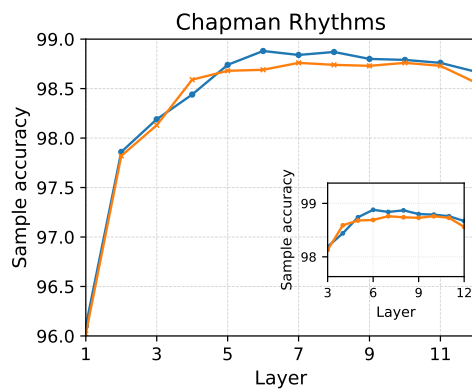
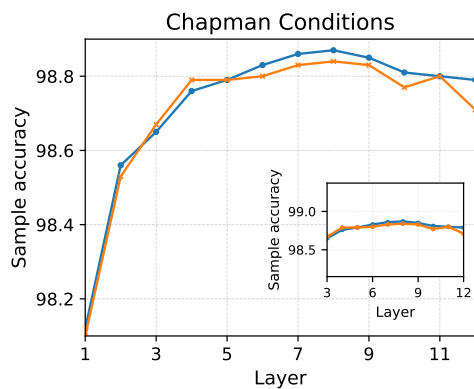
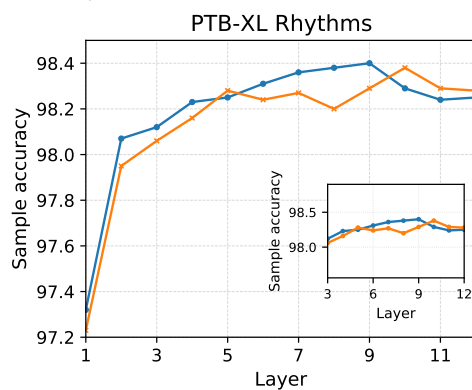
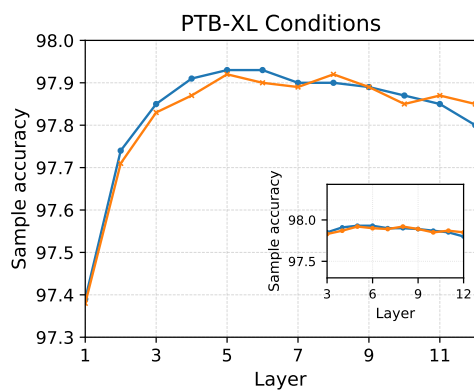
a) Macro AUC



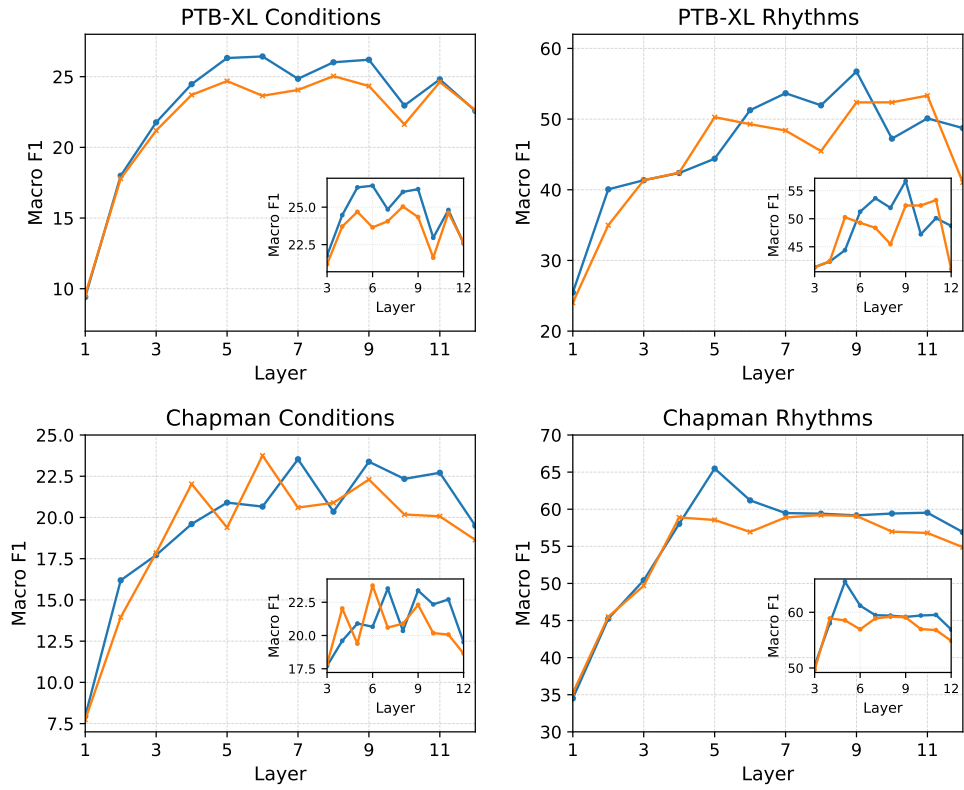
b) Sample AUC



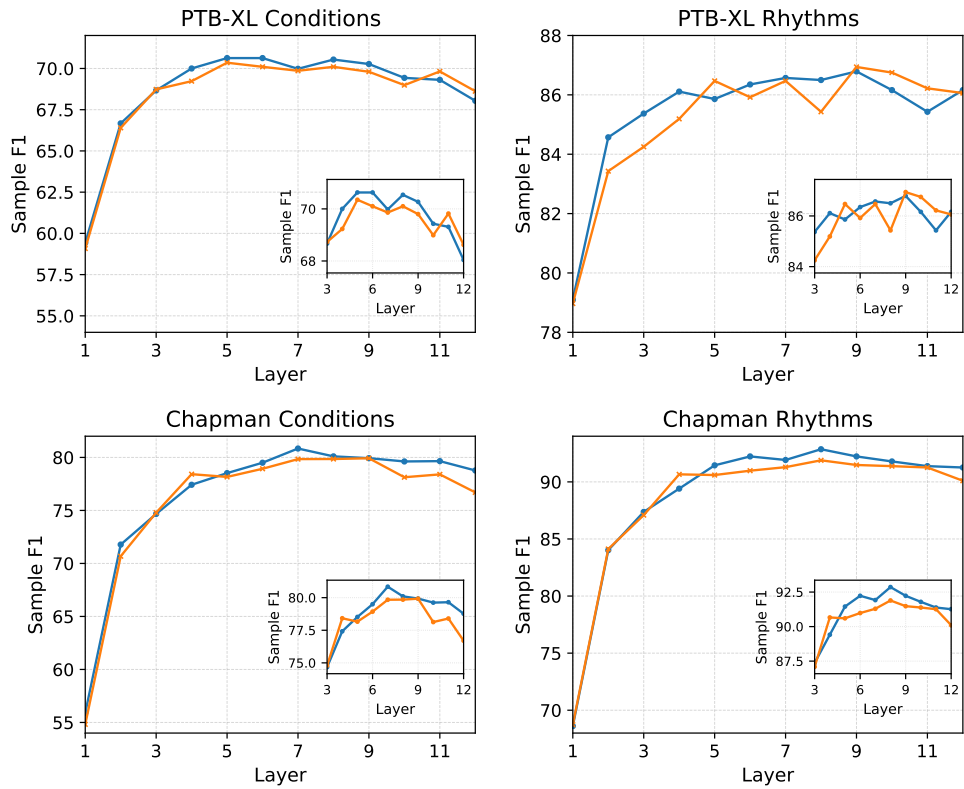
c) Instance accuracy



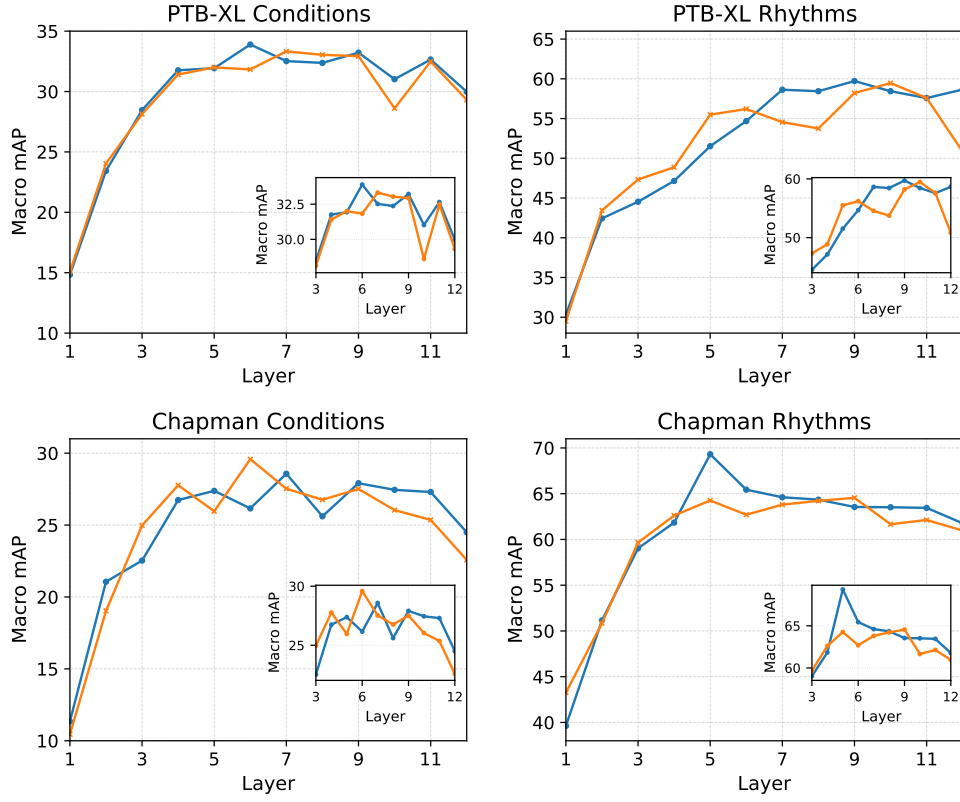
d) Sample accuracy



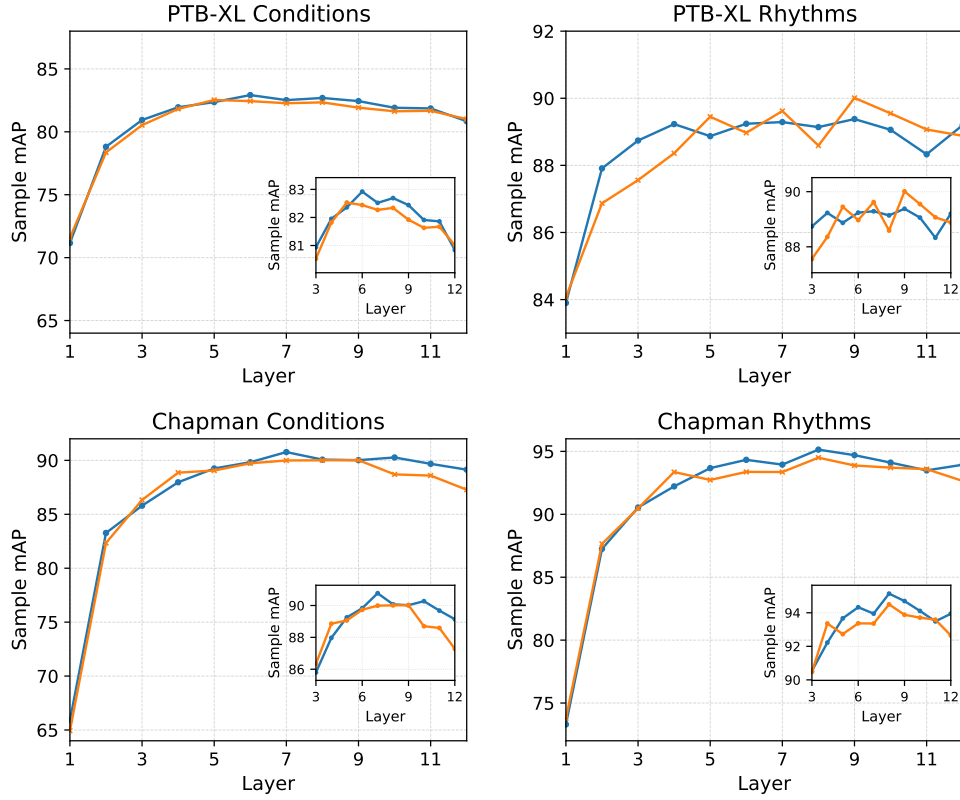
e) Macro F1 score



f) Sample F1 score



g) Macro mAP



h) Sample mAP

Fig. 9: Layer-wise Performance of STMEM vs IPASTMEM on PTB-XL Conditions, PTB-XL Rhythms, Chapman Conditions, and Chapman Rhythms. We train the classification head on top of representations from pre-trained ViT models for ECG condition and rhythm classification.